1

Solid State Research

1969

Prepared under Electronic Systems Division Contract AF 19(628)-5167 by

Lincoln Laboratory

MASSACHUSETTS INSTITUTE OF TECHNOLOGY

Lexington, Massachusetts

The work reported in this document was performed at Lincoln Laboratory, a center for research operated by Massachusetts Institute of Technology, with the support of the U.S. Air Force under Contract AF 19(628)-5167.

This document has been approved for public release and sale; its distribution is unlimited.

ABSTRACT

This report covers in detail the solid state research work at Lincoln Laboratory for the period 1 November 1968 through 31 January 1969. The topics covered are Solid State Device Research, Materials Research, and Physics of Solids.

Accepted for the Air Force
Franklin C. Hudson
Chief, Lincoln Laboratory Office

INTRODUCTION

I. SOLID STATE DEVICE RESEARCH

Guard-ringed GaAs Schottky barrier diodes have been fabricated which exhibit uniform avalanche photocurrent gains exceeding 100 with gain-bandwidth products over 50 GHz. The diodes consist of 5.3-mil diameter 100-Å thick semitransparent platinum Schottky barrier contacts electroplated on 2×10^{16} cm^{-3} n-type GaAs. The guard ring was formed by 400-keV proton radiation damage which generates an insulating region 4μ thick. Operating at a gain of 100 the photoresponse was uniform across the active region of the diode to better than ±20 percent, the response speed was less than 0.3 nsec and the improvement in signal to noise over low bias conditions was 34 dB.

Efficient doping of GaAs has been observed using Se^+ ions implanted at 400 keV, and high quality n-p junctions have been obtained using this technique. These junctions, formed by implantations into p-type material, had low leakage currents and a sharp reverse breakdown voltage of 24 V. Van der Pauw measurements indicate that a substantial fraction of the implanted ions are electrically active. Differential C-V measurements on gold Schottky barriers plated on implanted n-type samples gave a doping density curve which indicated that over half the implanted ions were electrically active.

Again using Se^+ ions implanted at 400 keV, n-p GaAs avalanche photodiodes have been fabricated which have photocurrent gains in excess of 300 when biased near reverse breakdown. As in the case of the Schottky barrier avalanche photodiodes a guard ring of insulating GaAs was formed by 400-keV proton bombardment. The 4.8-mil diameter diodes had typical reverse leakage currents of about 3×10^{-10} A at 1 V, and sharp reverse breakdowns at 24 V. Again the photoresponse was found to be uniform over the entire region of the diode to better than ±20 percent at an average photocurrent gain of 100.

Low angle (2° to 4° between {111} planes) grain boundaries which can behave as back-to-back diodes have been observed in n-type ZnSe. It is postulated that acceptor type states exist at the tilt grain boundary produced by the lattice mismatch which can act as electron traps creating a double depletion region. The surface states are sufficiently dense that the grain boundary behaves like two Schottky barrier diodes connected back-to-back. Under reverse breakdown visible light is emitted at these boundaries but with rather low, $\sim 5 \times 10^{-5}$, quantum efficiencies.

Epitaxial layers of GaAs have been grown in an $AsCl_3$-Ga-hydrogen flow system with 77°K Hall mobilities up to 210,000 cm^2/V sec, a significant improvement over the best previously known material. The best sample had a peak mobility of 340,000 cm^2/V sec at 40°K and a total ionized impurity concentration of about 1×10^{14} cm^{-3} which is approximately a factor of five improvement over previously reported values.

The effects of light on the charge state of anodized InSb MOS devices have been further classified. Infrared radiation in the energy range between 0.23 and 1.2 eV penetrates into the InSb and is absorbed, creating electron-hole pairs with insufficient energy to escape into the oxide. Starting

at about 1.2 eV some of the electrons photoexcited in the InSb escape and become trapped in the oxide. At photon energies in excess of about 3 eV electron-hole pairs are also generated in the oxide causing it to become photoconductive. By applying bias at these high photon energies the charge state of the oxide can be modified such that the surface of the n-type InSb can be swung from accumulation to depletion to inversion in a controlled fashion.

We have observed laser emission from diodes fabricated from the pseudo-binary alloy $Ph_{1-x}Sn_xSe$ in the composition range $0 \leqslant x \leqslant 0.279$ and have studied the composition and temperature dependence of the laser emission energy. For diodes fabricated from material with $x \geqslant 0.19$ the energy of the laser emission decreases as the temperature increases which is opposite to the situation in PbSe. This strongly supports the model in which the valence and conduction bands invert and exchange roles in the $Pb_{1-x}Sn_xSe$ alloy series as x is increased from 0 to 0.4.

We also have studied the magnetic field dependence of the laser emission energy in this alloy series in magnetic fields up to 50 kG. In the higher Sn content alloys with $x \geqslant 0.19$ the energy of the longest wavelength laser emission line decreases as the magnetic field is increased. This behavior is also opposite to the situation in PbSe and lends additional support to the band inversion model. This effect may also allow one to tune the laser emission to very long wavelengths using a magnetic field.

Interdiffusion in PbSe has been studied hy diffusing excess Se into Pb-rich n-type PbSe and excess Pb into Se-rich p-type PbSe. The motion of the resultant p-n or n-p junction as a function of time and temperature is in essential agreement with a diffusion model which assumes that the interdiffusion coefficient has two values, D_p in Se-rich material and D_n in Pb-rich material with $D_p = 9D_n$.

II. MATERIALS RESEARCH

Transparent, resistance-heated furnaces have been constructed for vapor crystal growth or other applications at temperatures up to 1000° to 1100°C. Conventional insulation is replaced by a layer of gold, deposited on Pyrex, which is highly reflecting in the infrared but thin enough (about 400 Å) to transmit in the visible.

Single crystals of $RbNiF_3$ have been grown from the melt by lowering a graphite crucible containing the compound, protected by an argon atmosphere, through an RF induction coil. The apparatus is also designed for the growth of ABF_3 crystals which require an HF atmosphere.

Compounds of the $CsBF_3$ type (B = Mn, Fe, Co, Ni, Zn, Cd, Mg) exist in four related close-packed structures, which range from entirely hexagonal to entirely cubic (perovskite). The proportion of cuhic close packing is found to increase with increasing size of the B-cation and with increasing hydrostatic pressure.

Optical ahsorption measurements have been used to determine the Te_2 partial pressure over condensed phases in the Bi-Te system as a function of composition and temperature. Solidus points for Bi_2Te_3 obtained from the pressure data are in good agreement with those calculated from Hall coefficient data by using the antistructure model for the stoichiometric defects.

Optical absorption measurements have been used to determine the partial pressures of Zn and Te over Zn-saturated and Te-saturated ZnTe, respectively, and to determine both pressures over ZnTe samples close to the congruently subliming composition. From the latter data, values of the equilibrium constant $p_{Zn}p_{Te_2}^{1/2}$ have been obtained for the range 960° to 1190°K.

Solidus curves for a number of semiconductor alloy systems have been calculated from the experimental liquidus curves by assuming that the deviations from ideality are comparable in the solid and liquid phases. For most of the systems, the calculated curves are in rather good agreement with the experimental solidus data, particularly for compositions not too close to the constituent with lower lattice constant.

X-ray scattering factors for aluminum have been obtained by means of absolute intensity measurements on cold-worked powder pellets. Except for the first two peaks, which are influenced hy solid state effects, the data are in good agreement with the results of relativistic Hartree-Fock calculations for the free atom, but not with those based on Slater's approximation to the exchange operator.

A method has been developed for determining the four major components in $(Pb_{1-x}Sn_x)(Te_{1-y}Se_y)$ alloys by electron microprobe analysis. An iterative procedure is used to obtain the correction factor for each element needed to calculate the atom fraction of the element from its measured X-ray intensity.

III. PHYSICS OF SOLIDS

Previous oscillatory magnetoreflection results on hismuth-antimony alloys in the range of composition $0 \leqslant \%\ Sb \leqslant 15$ have been complemented by measurements of additional alloys. Our measurements indicate the motion of some of the energy bands in the alloys and permit an identification of the L-point energy bands involved in transitions in pure hismuth with those involved in pure antimony. The results suggest a pattern for the variation of the energy bands at the L- and T-points in the Brillouin zone for the hismuth-antimony-arsenic system which is consistent with all previous magnetoreflection data in these semimetals.

As part of a program for studying the hand structure of the ferromagnetic semiconductor EuO, reflectance measurements have been carried out at photon energies between 1 and 11 eV at 300° and 77°K. Presently a Kramers-Kronig analysis is being performed in order to obtain the dielectric constant.

The 168 cm^{-1} ultraviolet-induced absorption line in AgBr, previously assigned to a 1s-2p transition of a bound polaron, has been examined in a magnetic field at liquid helium temperatures. A splitting, due to both the linear and quadratic Zeeman effect, has been ohserved.

A study has been initiated of electron tunneling through insulating films into PbSe with emphasis on the effects of the optic phonons. So far, the equipment has been checked out on GaAs; also preliminary measurements have been obtained in p-type PbSe.

The approach which was recently used to generalize the standard thermal Hartree-Fock approximation (STHFA) into a form, the thermal single determinant approximation (TSDA), for dealing

more satisfactorily with entropy in the zero-temperature limit, has now been applied to a boson system.

Measurements have been carried out on the magnetic field dependence (2.5 to 23.5 kOe) of the nuclear resonance linewidth of Mn^{55} in the low anisotropy antiferromagnetic compounds $CsMnF_3$ and $RbMnF_3$ at 18° and 4.2°K. An interpretation of the linewidth behavior in terms of existing theories gives fair agreement except for an unexplained anomalous linewidth peak which is observed only in $RbMnF_3$.

The spin-space group concept, advanced by Brinkman and Elliott for analyzing the symmetry properties of spin waves in magnetic insulators where spin-orbit coupling effects are negligible for the ground state of the magnetic ion, can be extended to optical excitons arising from single-ion transitions between the ground state and an excited state where spin-orbit effects are negligible. This idea has been applied to the $^4A_2 \rightarrow {}^2E$ excitons in Cr_2O_3 to investigate the role of spin-orbit coupling in producing the small but nonzero measured transfer-of-excitation matrix elements between opposite spin sublattices.

Using Brillouin spectroscopy, the velocity and attenuation of 27 to 28 GHz longitudinal hypersonic waves in fused quartz have been measured between 80° and 600°K. The pronounced attenuation peak at ~130°K, also observed previously by ultrasonic measurements but attributed to a structural relaxation mechanism, can be explained by a simple anharmonic mechanism involving scattering of thermal phonons.

Using exchange parameters obtained from two magnon Raman scattering and other magnetic measurements in $RbNiF_3$, a classical BPW calculation of the Curie temperature of $RbNiF_3$ has been performed. The calculated value of T_c is 135°K, compared with a measured value of 139°K. In addition, good agreement is obtained between calculations of sublattice magnetization above T_c in a magnetic field, and values inferred from NMR measurements.

It can be shown that for a Maxwellian electron gas the cross section for light scattering from single particle electron excitations is proportional to the electron distribution function under the conditions that (a) the momentum change imparted to the electron is large compared to the Debye wavelength and (b) the electrons have an infinite relaxation time. Experimental measurements in GaAs have confirmed these theoretical results.

The effect on the nonlinear refractive index of molecular interaction between anisotropic molecules in liquids has been investigated. Under certain restrictive conditions the liquid can be driven into a new ordered phase, similar to a liquid crystal mesophase.

CONTENTS

ORGANIZATION

SOLID STATE DIVISION

A. L. McWhorter, *Head*
P. E. Tannenwald, *Associate Head*
M. J. Hudson, *Assistant*
E. P. Warekois

SOLID STATE THEORY

H. J. Zeiger, *Leader*
M. M. Litvak, *Assistant Leader*

Brine, N. S.
Chinn, S. R.*
Dresselhaus, G. F.
Hamilton, D. C.
Hanus, J.
Kaplan, T. A.
Kleiner, W. H.
Landon, S. N.
Larsen, D. M.
Palm, B. J.†
Sigel, J. L.
Wilson, A. R. M.

OPTICS AND INFRARED

R. H. Kingston, *Leader*
R. J. Keyes, *Assistant Leader*

Bates, D. H.
Bostick, H. A.
Freed, C.
Gilmartin, T. J.
Hinkley, E. D.
Longaker, P. R.
McPhie, J. M.
O'Donnell, R. G.
Quist, T. M.
Ross, A. H. M.
Sullivan, F. M.
Swezey, L.
Zimmerman, M. D.

ELECTRONIC MATERIALS

J. B. Goodenough, *Leader*
A. J. Strauss, *Associate Leader*

Anderson, C. H., Jr.
Andrews, H. I.*
Arnott, R. J.
Banus, M. D.
Batson, D. A.
Brebrick, R. F., Jr.
Button, M. J.
Capes, R. N.
Delaney, E. J.
England, R. E.
Fahey, R. E.
Ferretti, A.
Finn, M. C.
Hilton, T. W.
Iseler, G. W.
Kafalas, J. A.
Kasper, H. M.
LaFleur, W. J.
Lavine, M. C.†
Longo, J. M.
Mastromattei, E. L.
O'Connor, J. R.
Owens, E. B.
Plonko, M. C.
Raccah, P. M.
Reed, T. B.
Roddy, J. T.
Searles, I. H.
Smith, F. T. J.
Stack, T. E.
Steininger, J. M.
Wheatley, G. E.

SOLID STATE PHYSICS

J. G. Mavroides, *Leader*
G. B. Wright, *Assistant Leader*

Allen, J. W.
Barch, W. E.
Blum, F. A.
Brandt, R. C.
Burke, J. W.
Crooker, P. P.
Dresselhaus, M. S.†
Dwight, K., Jr.
Feinleib, J.
Feldman, B.
Fulton, M. J.
Groves, S. H.
Henrich, V. E.
Johnson, E. J.
Kernan, W. C
Kolesar, D. F.
Krag, W. E.
Melngailis, J.
Menyuk, N.
Nill, K. W.
Parker, C. D.
Pine, A. S.
Scouler, W. J.
Strahm, N. D.*
Tichovolsky, E. J.*
Waldman, J.*
Weber, R.

APPLIED PHYSICS

J. O. Dimmock, *Leader*
T. C. Harman, *Assistant Leader*
I. Melngailis, *Assistant Leader*

Brueck, S.*
Calawa, A. R.
Carter, F. B.
Caswell, F. H.
Clough, T. F.
Donnelly, J. P.
Ferrante, G.
Foyt, A. G.
Lindley, W. T.
Mooradian, A.
Murphy, R. A.*
Oliver, M. R.*
Orphanos, W. G.*
Paladino, A. E.
Phelan, R. J., Jr.
Stillman, G. E.
Ward, J. H. R., III
Wolfe, C. M.
Youtz, P.

---

* Research Assistant
† Part Time

REPORTS BY AUTHORS ENGAGED IN SOLID STATE RESEARCH

15 November 1968 through 15 February 1969

PUBLISHED REPORTS

Journal Articles*

JA No.			
3210	Si-Te System: Partial Pressures of Te_2 and SiTe and Thermodynamic Properties from Optical Density of the Vapor Phase	R. F. Brebrick	J. Chem. Phys. 49, 2584 (1968)
3267	Spherical Model as the Limit of Infinite Spin Dimensionality	H. E. Stanley	Phys. Rev. 176, 718 (1968)
3274	Magnetic Resonance	R. Weber	Chapter 7, Magnetism and Magnetic Materials – 1968 Digest, H. Chang and T. R. McGuire, eds. (Academic Press, New York, 1968)
3284	Nonmetals	N. Menyuk	
3296	Photoconductivity in Single-Crystal $Pb_{1-x}Sn_xTe$	I. Melngailis T. C. Harman	Appl. Phys. Letters 13, 180 (1968)
3328	Polymorphism in Silver Telluride at High Pressures and Temperatures	M. D. Banus M. C. Finn	J. Electrochem. Soc. 116, 91 (1969)
3347	Exchange Interactions and Raman Scattering from Spin Excitations in $RbNiF_3$	S. R. Chinn H. J. Zeiger	Phys. Rev. Letters 21, 1589 (1968)
3353	$LnCrTeO_6$ – A New Series of Compounds Based on the $PhSb_2O_6$ Structure	H. M. Kasper	Materials Research Bull. 4, 33 (1969)
MS-2221	Influence of the Molecular Interaction on the AC Kerr Effect: Possibility of a Field-Induced Phase Transition	J. Hanus	IEEE J. Quant. Electron. QE-4, 753 (1968)

UNPUBLISHED REPORTS

Journal Articles

JA No.			
3301	Effective Mass Theory for Polarons in External Fields	D. M. Larsen	Accepted by Phys. Rev.

*Reprints available.

Reports

JA No.			
3304	Self-Modulation, Self-Steepening and Spectral Development of Light in Small Scale Trapped Filaments	T. K. Gaustafson* J-P. Taran* H. A. Haus* J. R. Lifsitz* P. L. Kelley	Accepted by Phys. Rev.
3308	Conditions for Microwave Radiation from Excited OH Λ-Doublet States	M. M. Litvak B. Zuckerman* D. F. Dickinson*	Accepted by Astrophys. J.
3317A	Fermi Surface and Optical Properties of Copper	G. F. Dresselhaus	Accepted by Solid State Commun.
3320	Single Crystal Lead-Tin Chalcogenides	I. Melngailis T. C. Harman	Accepted as chapter in Semiconductors and Semimetals, Vol. 7 (Academic Press, New York)
3335	A Transport Equation for Interacting Fermions in Random Scattering Centers. I. A Quasiparticle Description in the Macroscopic and Low Temperature Limit	J. L. Sigel P. N. Argyres	Accepted by Phys. Rev.
3340	Infrared Pumping of Interstellar OH	M. M. Litvak	Accepted by Astrophys. J.
3346	A New Series of Rare Earth Garnets $Ln_3^{+3}M_2Li^{+1}O_{12}$(M = Te,W)	H. M. Kasper	Accepted by Inorg. Chem.
3365	Photoluminescence of Metals	A. Mooradian	Accepted by Phys. Rev. Letters
3386	Transient and Steady State Thermal Self-Focusing	R. L. Carman* A. Mooradian P. L. Kelley A. Tufts	Accepted by Appl. Phys. Letters
3387	Infrared Transmission, Magnetic Birefringence and Faraday Rotation in EuO	J. O. Dimmock C. E. Hurwitz T. B. Reed	Accepted by Appl. Phys. Letters
3394	Far Infrared and Submillimeter Impact Ionization Modulator	I. Melngailis P. E. Tannenwald	Accepted by Proc. IEEE (Letters)
3411	International Conference on Silicon Carbide (A Conference Report)	J. R. O'Connor	Accepted by J. Crystal Growth

* Author not at Lincoln Laboratory.

Meeting Speeches*

MS No.			
2316A	A Phase Diagram for Electrons in Solids	J.B. Goodenough	Seminar, IBM Watson Research Center, Yorktown Heights, New York, 12 December 1968
2331A	Raman Scattering from Spin-Density Fluctuations in n-GaAs	D.C. Hamilton	Solid State Conference, University of California, 13-17 January 1969
2362A	The High-Pressure Forms of $CsNiF_3$	J.M. Longo J.A. Kafalas	Magnetism and Magnetic Materials Conference, New York, 18-21 November 1968
2374	Distant-Neighbor B-B Interactions in Cobalt Chromite	K. Dwight N. Menyuk	
2377	On the Critical Behavior of Quantum Mechanical Heisenberg Ferro- and Antiferromagnets	H.E. Stanley	
2378	Critical Indices for a System of Spins of Arbitrary Dimensionality Situated on a Lattice of Arbitrary Dimensionality	H.E. Stanley	
2380	Pressure Effect Measurements Using a Vibrating-Coil Magnetometer	N. Menyuk J.A. Kafalas K. Dwight J.B. Goodenough	
2384	Band Structure of Magnetic Semiconductors	D. Adler† J. Feinleib	
2385	Optical Studies and Band Structure of Cu-Ni Alloys	J. Feinleib W.J. Scouler J. Hanus	
2389	Raman Scattering by Magnetic Excitations in $RbNiF_3$	S.R. Chinn H.J. Zeiger	
2391	Ultrasonic Propagation in EuO	Y. Shapira† T.B. Reed	
2415A	Infrared Transmission, Magnetic Birefringence and Faraday Rotation in EuO	J.O. Dimmock C.E. Hurwitz T.B. Reed	
2387A	A New Thermal Hartree-Fock Approximation and Some Consequences	T.A. Kaplan P.N. Argyres	International Symposium on Atomic, Molecular, and Solid-State Theory and Quantum Biology, Sanibel Island, Florida, 13-18 January 1969
2470	Experimental Charge Density of Al	P.M. Raccah V.E. Henrich	

* Titles of Meeting Speeches are listed for information only. No copies are available for distribution.

† Author not at Lincoln Laboratory.

Reports

MS No.			
2415	Infrared Transmission, Magnetic Birefringence and Faraday Rotation of EuO	J. O. Dimmock C. E. Hurwitz T. B. Reed	American Physical Society, Miami Beach, Florida, 25-27 November 1968
2420D	Light Scattering from Electrons in Solids	A. Mooradian	Seminar, Bell Telephone Laboratories, Holmdel, New Jersey, 7 January 1969
2420E	Light Scattering from Semiconductors	A. Mooradian	Seminar, University of California, 17 January 1969
2425	Raman Scattering from InSb and InAs Surfaces	K. W. Nill A. Mooradian	American Physical Society, San Diego, California, 18-20 December 1968
2458	The Maser Physics of Interstellar OH	M. M. Litvak	
2426, 2426A	Laser Light Scattering Studies in Solids	A. Mooradian	Industrial Liaison Symposium, M. I. T., 18 December 1968; Seminar, Raytheon Company, Waltham, Massachusetts, 12 February 1969
2441	Interference Magnetoreflection Studies in InSb	P. W. Staecker* M. S. Dresselhaus S. Iwasa*	
2443	A Transport Equation for Interacting Fermions in Random Scattering Centers. I. A Quasiparticle Description in the Macroscopic and Low Temperature Limit	J. L. Sigel P. N. Argyres	American Physical Society, New York, 3-6 Fehruary 1969
2490	Effects of Electron-Phonon Interaction on Electronic Energy Levels	D. M. Larsen	
2445	The Fundamental Absorption Edge of Semiconductors	E. J. Johnson	Seminar, Boston College, 20 November 1968
2447	A New Look at the Fermi Surface	G. F. Dresselhaus	Colloquium, Yeshiva University, 18 November 1968
2450	Magnetic Critical Phenomena	H. E. Stanley	Colloquium, M. I. T., 22 November 1968
2451, 2451A, 2451B, 2451C	A New Look at the Fermi Surface	G. F. Dresselhaus	Seminar, Northeastern University, 26 November 1968; Seminar, National Magnet Laboratory, 11 December 1968; Seminar, Raytheon Company, Waltham, Massachusetts, 29 January 1969; Seminar, University of California, 20 January 1969

* Author not at Lincoln Laboratory.

MS No.			
2468	Finite Temperature Single-Determinant Theory	T. A. Kaplan	Seminar, Wesleyan University, 18 December 1968
2496	Pitfalls, Detours and Shortcuts on the Road to Single Crystal Growth	T. B. Reed	Electrochemical Society, Lexington, Massachusetts, 14 January 1969

I. SOLID STATE DEVICE RESEARCH

A. GaAs SCHOTTKY BARRIER AVALANCHE PHOTODIODES

Guard-ringed GaAs Schottky barrier diodes were made which exhibit uniform avalanche photocurrent gains exceeding 100 with gain-bandwidth products over 50 GHz. Although there has been considerable development of p-n junction avalanche photodetectors since Johnson's[1] demonstration of enhanced signal-to-noise ratio in Si diodes, we believe this is the first report of avalanche photogain observed in GaAs Schottky barrier diodes.

Previous work on diode avalanche photodetectors has shown that, in order to achieve substantial avalanche gain in the center of the diode, the premature breakdown caused by high fields at the edge of the diode must be eliminated. In silicon Schottky barrier devices,[2] this has been done using a diffused guard ring around the perimeter of each diode. We have developed two different techniques, one using epitaxial growth[3] and one using proton bombardment[4] for fabricating the necessary guard ring for GaAs Schottky barrier diodes. In both cases, the perimeter of the diode is located over a region of lower carrier concentration material, preventing premature breakdown at the edge of the diode.

Figure I-1 shows a cross section of the diode structure used to obtain the results reported here. The GaAs substrate was n-type with a carrier concentration of $2 \times 10^{16}/cm^3$. The 5.3-mil diameter 100-Å thick semitransparent platinum Schottky barrier contact and the attached bonding pad were electroplated through holes in SiO_2 and subsequently covered with an additional 1500 Å of SiO_2 to protect the thin metal layer. The center of each diode was covered with a thick 5-mil diameter circle of photoresist, and then the sample was bombarded with 400-keV protons. Proton radiation penetrates into the GaAs, except in the circular regions protected by the photoresist, and creates a 4-μ thick high resistivity surface layer providing the guard ring. Following this step, the SiO_2 was removed from the rim of the diode and the bonding pad, and additional gold was electroplated to lower the contact resistance. The 5-mil photoresist circles were then removed from the center (active) region of the diodes.

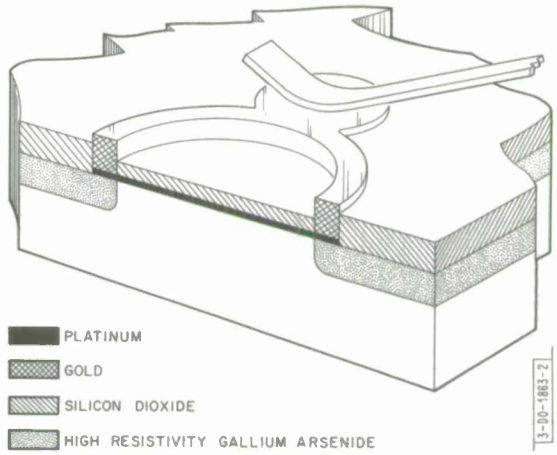

Fig. I-1. Cross section of avalanche Schottky barrier photodiode structure.

The photoresponse of these diodes was evaluated by scanning each diode with a 3-μm diameter light spot from a HeNe laser, and displaying the scanned photoresponse on an oscilloscope.[5] For diodes fabricated as above, the zero bias quantum efficiency was typically 30 percent with a variation of less than ±10 percent across the active area of the diode. Operating the diodes at an average gain of 100, the variation in response was less than ±20 percent.† As a further test

† In similar diodes which did not have a guard ring, breakdown occurred at the perimeter. These diodes have exhibited gains as large as 10^5 in the depletion region near the perimeter; however, they had long response times (10^{-3} sec).

of uniformity, several diodes were biased into avalanche breakdown, and the emitted visible light was observed. As expected, the emitted light was essentially uniform over the active region of the diode.

The gain-bandwidth product of these diodes was evaluated by measuring the response time of the photocurrent to a pulsed GaAsP diode laser. At an operating gain of 100, the measured fall time of 0.3 ns yields a gain-bandwidth product of 50 GHz. An accurate determination of the rise time could not be made because of uncertainties in the shape of the light pulse. However, the observed 0.1-ns rise time of the photocurrent to a flat top suggests that the photodiode has an even larger gain-bandwidth product than that corresponding to the fall time, and that the fall time is primarily due to the turnoff of the diode laser.

In Fig. I-2 we show the system noise measured at 30 MHz as a function of the observed photocurrent multiplication for a diode driving an amplifier with a 50-ohm input and a noise figure of 2.5 dB. The noise power is plotted as a ratio of the observed noise to the thermal noise of the 50-ohm input resistance, with the excess noise at low values of multiplication caused by the amplifier. As may be seen, substantial signal multiplication can be achieved before an increase in noise is observed. Since the signal power is amplified as M^2, an improved signal-to-noise ratio for this system is obtained until the noise power is also increasing as M^2. At higher values of multiplication, the noise increases faster than the signal. The maximum improvement in signal-to-noise ratio was 34 dB, which occurred at a multiplication of 100.

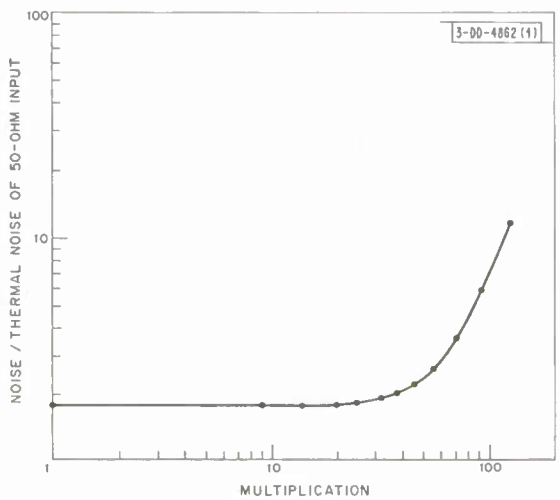

Fig. I-2. Noise power (measured at 30 MHz) as a function of photocurrent multiplication, for an avalanche Schottky barrier photodiode.

In addition to these measurements in a 50-ohm system, we have measured the diode noise at 100 kHz with a 1000-ohm load resistor. For the range of multiplication between 5 and 120, the noise power increased as $M^{2.1}$. This result is in contrast to the results for Ge[6] (Ref. 6) and Si (Refs. 7, 8) p-n junction avalanche photodiodes where the noise power was observed to increase as M^3 and $M^{2.5}$ respectively. Our result, if interpreted using McIntyre's model,[9] which predicts that the noise power will vary as M^3 if the hole and electron ionization rates are equal and as M^2 if one rate is much greater than the other, suggests that there is a substantial difference in the hole and electron ionization rates.

We have also studied the spectral response of these diodes at various bias levels. Figure I-3 shows the response of a 20-mil diameter diode at two bias levels. The actual response at 40 volts was much greater than at 10 volts; however, these curves have been normalized to coincide for wavelengths shorter than 0.86 μm. These curves thus reveal an increase in photoresponse with bias which is greater for wavelengths longer than 0.86 μm than for wavelengths less than 0.86 μm. The increase in width of the depletion region from 1 to 2 μ with an increase in bias from 10 to 40 volts, could be expected to increase the relative response for this longer wavelength penetrating light up to a factor of two, which, however, is not enough to explain the data.

A similar difference in the relative response to short and long wavelength photons observed in Ge (Ref. 10), Si (Ref. 11) and GaAs (Ref. 12) p-n junction avalanche diodes has been explained in terms of a change in the dominant carrier being swept into the avalanching region. The ratio of electron and hole ionization rates in these materials has been calculated from these experiments. However, for Schottky barrier diodes where the highest field region is at the metal-semiconductor interface, essentially all of the light is absorbed on the semiconductor side of the avalanching region and the argument concerning the ratio of ionization rates does not simply follow.

In order to investigate another possible reason for the increased relative response, the absorption through a diode was measured and is also shown in Fig. I-3. In this experiment, a 10-mil diameter area in the center of the 20-mil diameter diode was illuminated and the amount of light penetrating through the high field depletion region and the additional 300 μm of bulk GaAs was measured. For wavelengths longer than about 0.92 μm, the observed change in absorption with bias completely accounts for the increase in the relative response of the diode. For shorter wavelengths, although bulk absorption obscures the changes which occur in the depletion region, the variation in photoresponse is still in qualitative agreement with a change in absorption in the depletion region. We have not studied the causes of this change in absorption with bias. However, the effect is similar in both magnitude and wavelength variation to that seen in GaAs p-n junction diodes by Penchina[13] et al., who explained their results on the basis of the Franz-Keldysh effect.

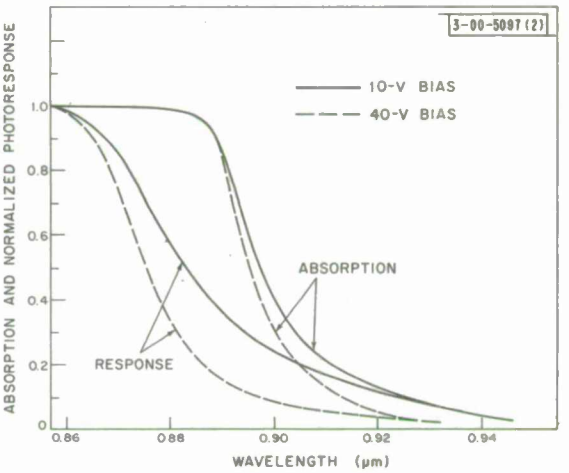

Fig. I-3. Spectral variation of the photoresponse and absorption of Schottky barrier photodiode at two different bias levels.

W. T. Lindley C. M. Wolfe
R. J. Phelan, Jr. A. G. Foyt

B. EFFICIENT Se DOPING OF GaAs BY ION IMPLANTATION

We have observed efficient doping of GaAs using Se^+ ions implanted at 400 keV, and have also obtained high quality p-n junctions using this technique. The Se^+ ions were produced by the RF excitation of hydrogen selenide, accelerated to 400 keV in a Van de Graaff generator and magnetically analyzed. Both p- and n-type GaAs substrates were used. Prior to implantation the samples were coated with ~1500 Å of SiO_2. Each sample was heated to 500°C during implantation and subsequently annealed at 800°C for 1 minute. In p-type samples ($p \sim 3 \times 10^{16}/cm^3$), a dose of $2 \times 10^{13}/cm^2$ produced type conversion and p-n junctions. These p-n junctions had low leakage currents, with a sharp reverse breakdown voltage of 24 volts. Van der Pauw[14] measurements on these samples indicate that a substantial fraction of the implanted ions are electrically active. In n-type samples ($n \sim 10^{16}/cm^3$), the doping profile of the implanted region was obtained using standard differential capacitance-voltage measurements on gold plated

Schottky barriers.[15] In Fig. I-4 we show the profile resulting from a Se^+ dose of $3 \times 10^{12}/cm^2$. As may be seen, a peak concentration of $2 \times 10^{17}/cm^3$ with a standard deviation of about 500 Å was observed. The integrated doping density shows that over half of the implanted ions are electrically active.

A. G. Foyt
J. P. Donnelly
W. T. Lindley

C. ION IMPLANTED GaAs AVALANCHE PHOTODIODES

Using Se^+ ions implanted at 400 keV n-p GaAs diodes were fabricated which have photocurrent gains in excess of 300 when biased near reverse breakdown. The p-type GaAs substrates ($p \sim 2 \times 10^{16}/cm^3$) were implanted with a dose of $2 \times 10^{13}/cm^2$ Se^+ ions and subsequently annealed to give an n-type layer ~0.3-μ thick with a sheet resistance of approximately 400 ohms/square. Following implantation, thin (1000 Å) gold-tin contact rings with an inner diameter of 4.8 mils and a width of 0.2 mil were plated on the implanted layer using SiO_2 as a plating mask. Platinum was plated over the rings and the contacts alloyed at 360°C. The GaAs around each diode was converted to high resistivity material using proton bombardment, with the interior of each ring protected from the proton beam with photoresist. This high resistivity layer separated the diodes and served as a guard ring which prevents edge breakdown. The resulting diode structure is shown in Fig. I-5. These diodes had typical reverse leakage currents of about 3×10^{-10} A at 1 volt, and sharp reverse breakdowns at 24 volts.

The uniformity of these diodes was investigated by scanning each diode with a 3-μ light spot from an HeNe laser and displaying the photocurrent response on an oscilloscope. These measurements showed that the entire diode area was active, and that the variation in photoresponse was less than ±20 percent at an average photocurrent gain of 100.

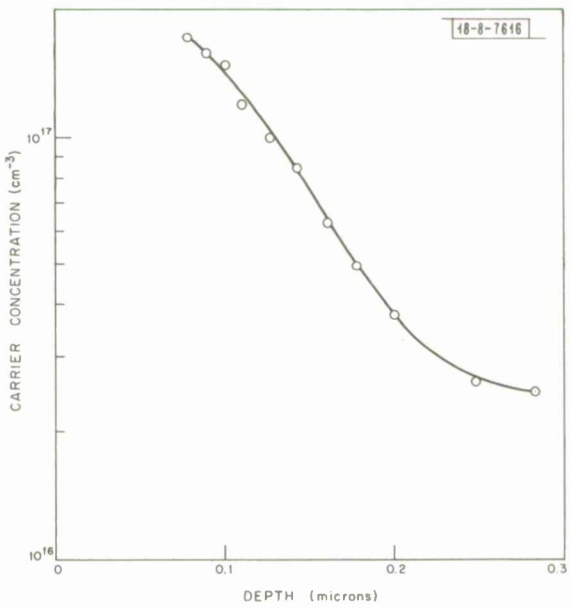

Fig. I-4. Carrier concentration profile for n-GaAs ($n = 2 \times 10^{16}/cm^3$) sample implanted with $3 \times 10^{12}/cm^2$ Se^+ ions at 400 keV.

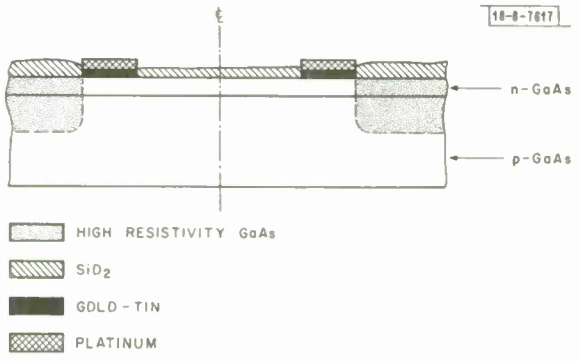

Fig. I-5. Cross section of n-p junction avalonche photodiode structure.

Initial speed measurements were made by using a pulsed GaAsP light emitting diode. At a photocurrent gain of 100, the rise and fall times of the photodiode were less than $\frac{1}{4}$ μs, which is the limit of the light emitting diode.

W. T. Lindley A. G. Foyt
J. P. Donnelly R. J. Phelan, Jr.

D. AVALANCHE BREAKDOWN AND LIGHT EMISSION AT GRAIN BOUNDARIES IN n-ZnSe

We have recently observed that low angle grain boundaries in n-ZnSe can behave as back to back diodes. This behavior is similar to that observed at grain boundaries in n-Si and Ge.[16-18] In ZnSe, avalanche breakdown occurs when the grain boundary is biased to approximately 20 volts in either direction. This breakdown is accompanied by broad visible electroluminescence

The ZnSe crystals used were grown by an open tube vapor transport of the constituent elements. Hydrogen purified by a palladium alloy filter was passed in separate streams over two heated boats containing 99.999 percent pure Zn and Se, respectively. The resulting vapor streams were combined in a uniform temperature region where growth occurred. Crystals grown at 1100°C consisted of plates (approximately 5 × 5 × 1 mm) of the cubic modification, having ⟨111⟩ surfaces. These were polished and etched into platelets approximately 0.25-mm thick. Since this as-grown ZnSe exhibited high resistivity even after being annealed in excess Zn at 1050°C, indium was diffused into the samples under a Zn atmosphere at 1000°C. Hall measurements on single crystal portions of these diffused samples indicated an n-type carrier concentration of $10^{16}/cm^3$ and a mobility of 160 cm^2/volt-sec.

Several Hall samples were found to contain a low angle grain boundary as shown schematically in Fig. I-6. The current-voltage characteristics between any pair of contacts on the same side of the grain boundary showed ohmic behavior with a resistance of approximately 250 ohms. Between contacts on opposite sides of the grain boundary, back to back diode characteristics as shown in Fig. I-7 were observed. With a few mA of current flowing in either direction, visible

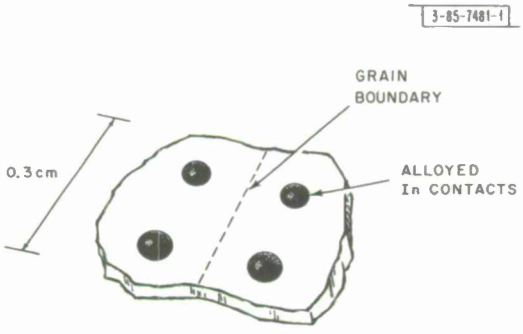

Fig. I-6. Typical ZnSe sample with four contacts, two on either side of grain boundary.

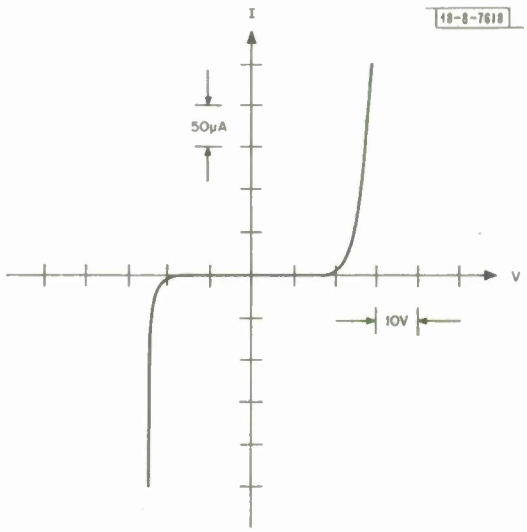

Fig. I-7. Current-voltage characteristics of low angle grain boundary in cubic n-type ZnSe.

-85-7484-1

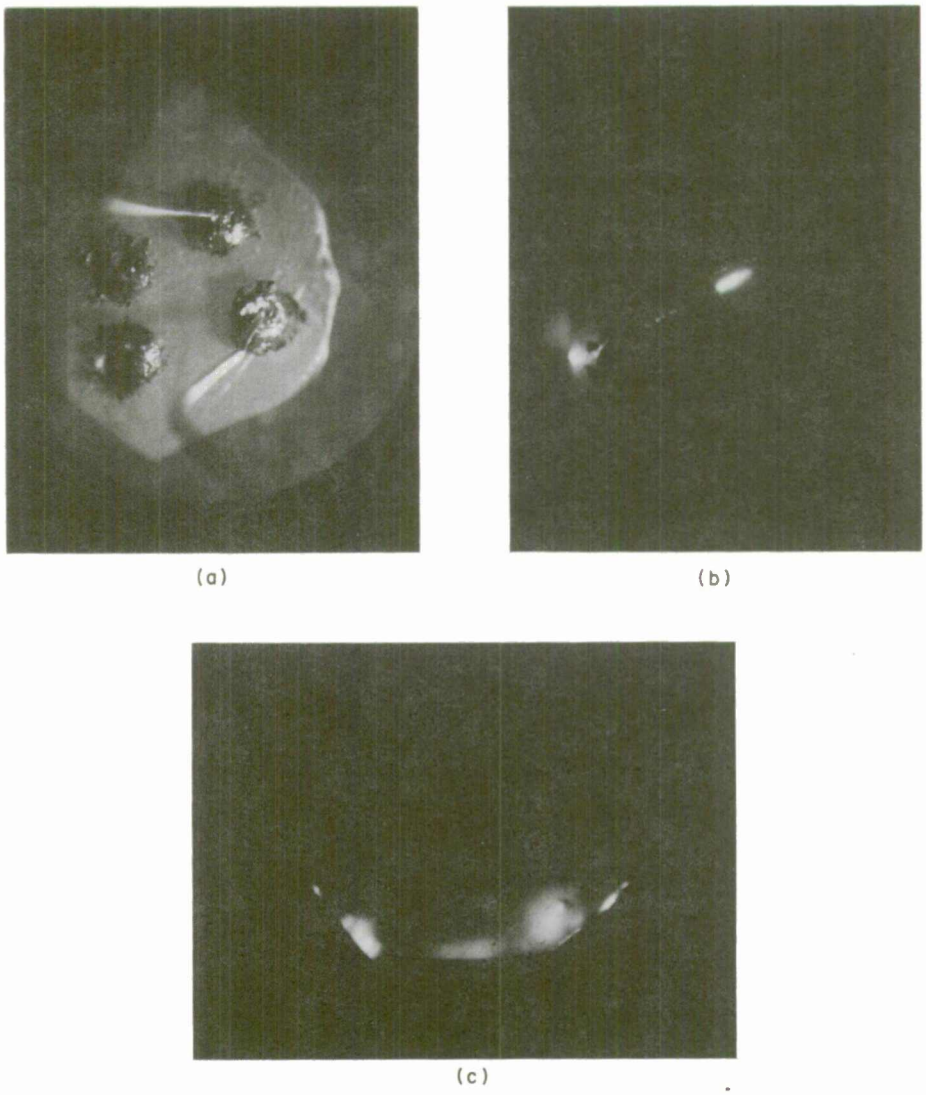

(a) (b)

(c)

Fig. I-8. Light emission along groin boundary. (a) Typicol ZnSe groin boundory sample; (b) light emitted olong grain boundory when biosed into ovolanche; (c) another ZnSe sample in which light is emitted from three connected stroight line segments.

light emission was observed along the grain boundary as illustrated in Figs. I-8(a) and (b). On close investigation, the light appeared to come from distinct filaments within the boundary. As additional current was passed through the sample, the light from some filaments appeared to saturate and additional filaments lit up. On another sample, light was emitted from several connected straight line segments, as shown in Fig. I-8(c). X-ray analysis has substantiated that a low angle tilt grain boundary (2° to 4° between {111} planes) exists at the plane from which the light is emitted.

Based on this experimental evidence, it is postulated that acceptor type "surface states" exist at the tilt grain boundary. The slight tilt misorientation results in a network of edge dislocations and therefore "dangling bonds" which can act as acceptors.[18,19] There is also the possibility of a segregation of deep acceptor impurities to the grain boundary. In any event these surface states trap mobile electrons creating a double depletion region as depicted in the band diagram of Fig. I-9(a).

The surface states are of a sufficient density that the grain boundary can be approximately treated as two separate Schottky barriers connected back to back.[16-18] With an applied voltage, one diode is forward biased while the other is reverse biased. Therefore, when the applied voltage is greater than several kT, almost the entire voltage drop occurs across the reverse biased portion of the grain boundary as shown in Fig. I-9(b). Additional electrons are trapped by the surface states to maintain charge neutrality.

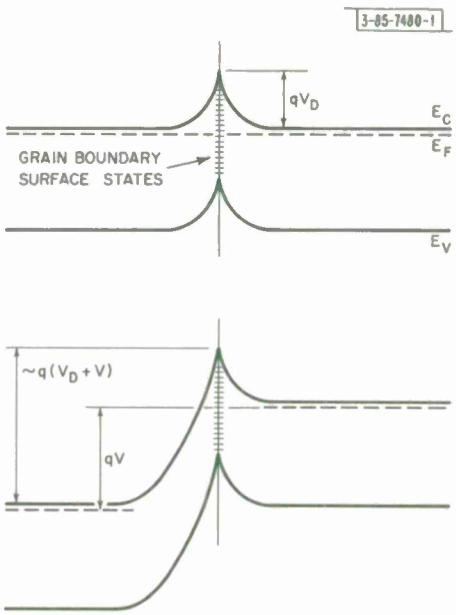

Fig. I-9. Band diagram of grain boundary in n-ZnSe. (a) At equilibrium; (b) with applied voltage V.

Differential capacitance-voltage measurements indicate that this model is essentially correct. The capacitance is a maximum at zero bias and decreases monotonically as the voltage is increased in either direction. Above several volts in either direction, $1/C^2$ is a linear function of the voltage. From the slope, one can calculate a constant carrier concentration of approximately $7 \times 10^{15}/cm^3$. This compares favorably with the $10^{16}/cm^3$ obtained by Hall measurements.

The sharp breakdown characteristics (Fig. I-7) and the filamentary nature of the light emission indicate that these grain boundaries break down by an avalanche mechanism. The spectrum of the emitted light is very broad at both 77°K and 300°K as shown in Fig. I-10. This electroluminescence was visible in ordinary room light with only 20 mA flowing through a grain of approximately $8 \times 10^{-3} cm^2$. Using current pulses of approximately 0.3 μs duration and a calibrated photomultiplier with an S-1 surface, the quantum efficiency was found to be superlinear out to currents of approximately 1 ampere, where irreversible damage occurred. Even at these currents, however, the external quantum efficiency was only about 5×10^{-5} at 300°K and only a factor of two

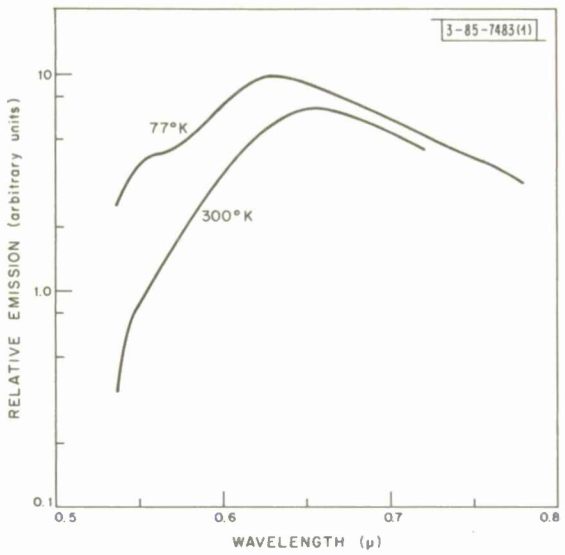

Fig. I-10. Spectrum of avalanche electroluminescence at grain boundary in n-ZnSe.

higher at 77°K. Shorter pulses were not used because of an electroluminescent risetime of approximately 0.1 μs which was inherent in these ZnSe devices.

In conclusion, it was found that low angle grain boundaries can create high resistance regions in ZnSe. Although visible electroluminescence was obtained by the avalanche breakdown of these boundaries, the quantum efficiency was low. At present, these grain boundaries are a source of trouble in working with cubic ZnSe, especially in lower concentration materials where the breakdown voltage of the grain boundaries is higher.

J. P. Donnelly
F. T. J. Smith

E. HIGHER PURITY EPITAXIAL GaAs

The first significant improvement in the purity of epitaxial GaAs was obtained by a vapor-phase $AsCl_3$-Ga flow system with a reported 77°K mobility of about 40,000 cm^2/V sec.[20,21] Using the same system, other workers soon thereafter attained 77°K mobilities of 54,000 cm^2/V sec,[22] 70,000 cm^2/V sec,[23] and 106,000 cm^2/V sec.[24] A similar improvement was then achieved in liquid-phase epitaxy with 77°K mobilities of 95,000 cm^2/V sec[25] and 106,000 cm^2/V sec[26] using a GaAs-Ga system. Recently,† 77°K mobilities as high as 130,000 cm^2/V sec have been reported for both the $AsCl_3$-Ga vapor-phase and the GaAs-Ga liquid-phase epitaxial systems. Here we report epitaxial layers grown in an $AsCl_3$-Ga flow system with 77°K mobilities up to 210,000 cm^2/V sec.

Some properties of these epitaxial layers are listed in Table I-1. Carrier concentrations and mobilities were determined from Hall constants which were measured in a magnetic field

† At the 1968 International Conference on Gallium Arsenide in Dallas, Texas.

TABLE I-1
PROPERTIES OF EPITAXIAL GALLIUM ARSENIDE

$n_{300°K}$ (cm^{-3})	$\mu_{300°K}$ ($cm^2/V\,sec$)	$\mu_{77°K}$ ($cm^2/V\,sec$)	Thickness (μ)
1.8×10^{13}	8200	180,000	80
2.8×10^{13}	8100	210,000	68
3.8×10^{13}	7600	190,000	54
2.6×10^{13}	7800	195,000	68
3.1×10^{13}	8200	190,000	45

of 12 kG. The 77°K mobilities of these samples are close to the 200,000 $cm^2/V\,sec$[24] estimated limit for lattice scattering at this temperature. The Hall constant and resistivity of several samples were measured as a function of temperature with the best sample having a peak mobility of 340,000 cm^2/V sec at 40°K. Analysis of the temperature dependence of the Hall constant and the mobility indicate a total ionized impurity concentration of about $1 \times 10^{14} cm^{-3}$ which is approximately a factor of 5 improvement over previously reported values. This improved purity was obtained with commercially available starting materials and techniques previously described.[27]

C. M. Wolfe
G. E. Stillman
W. T. Lindley
L. Krohn, Jr.
J. O. Dimmock

F. EFFECTS OF LIGHT ON THE CHARGE STATE OF InSb MOS DEVICES

It has been shown[28] that InSb MOS structures can be used to store optical images which can be nondestructively read out with a scanning light beam and also erased with light. The storage, reading and erasure were accomplished by using three wavelengths of light: white light from a tungsten lamp for storing the images, infrared for reading the image, and ultraviolet light from a mercury lamp for erasure. To measure the wavelength intervals for each effect and to pursue the mechanisms involved, we have made a detailed study of the effects on the InSb MOS devices of photon radiation in the energy range between 0.5 and 5.0 eV. The light induced charge transfers occurring within the structure were discussed in a previous report;[29] the present report summarizes the mechanisms involved and presents some of the spectral data obtained.

The device structure consists of a sample of InSb, one surface of which is anodized to form an oxide layer about 500 Å thick and a semitransparent nickel film about 100 Å thick is evaporated onto the oxide layer[30] to form a metal-oxide-semiconductor sandwich or "MOS" structure. Initial studies[30] at 77°K using n-type InSb showed that infrared radiation of wavelengths from one to 5.4 μ would penetrate the metal and the oxide and be absorbed in a depletion region in the InSb at the oxide-InSb interface. The light absorbed in the depletion region generates

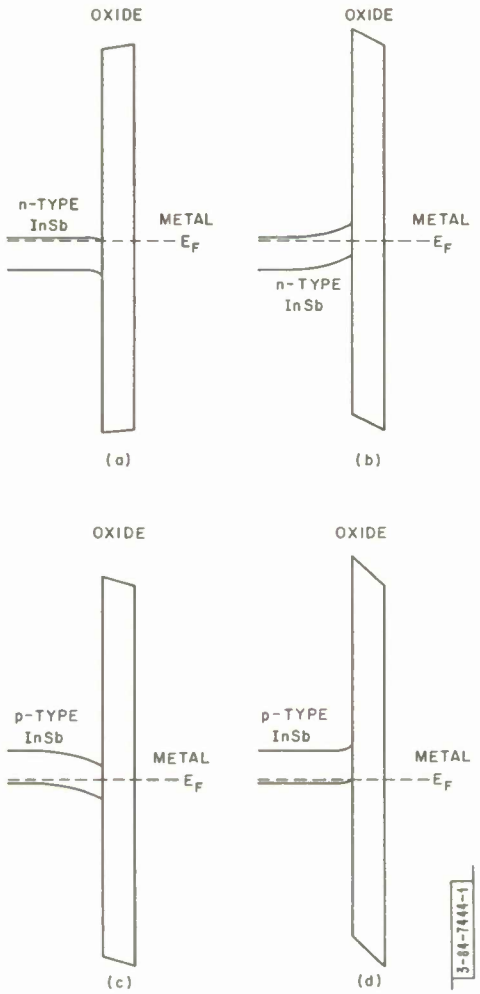

Fig. I-11. Model for band edges in the InSb-MOS devices. (o) n-type InSb with an accumulotion regian; (b) n-type InSb with o depletion layer; (c) p-type InSb with a depletion layer; (d) p-type InSb with an occumulation loyer.

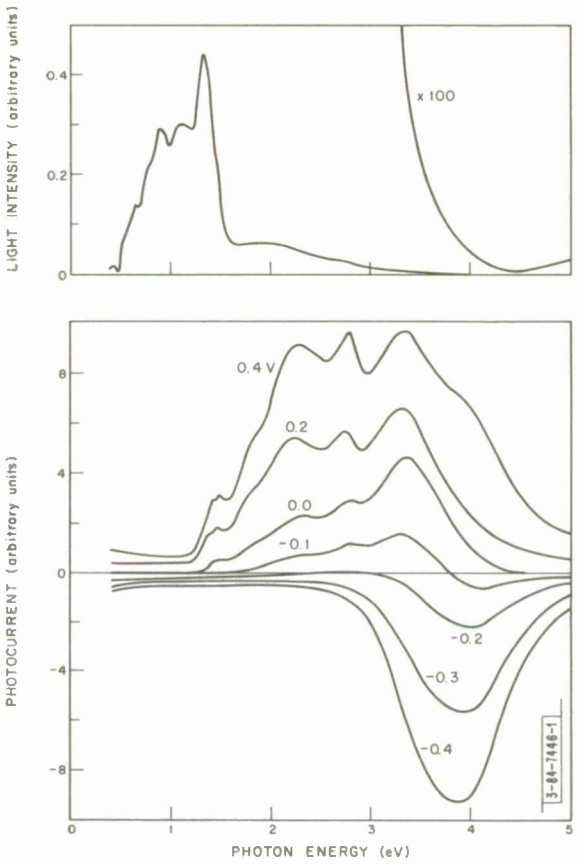

Fig. I-12. Unnormalized photocurrent versus photon energy with different opplied bioses far n-type InSb-MOS devices. Applied biases ore indicated on curves. Top curve indicotes light intensity which decreases by ≈ 4 orders of mognitude between 1.8 ond 5 eV.

electron-hole pairs which result in a photovoltage appearing across the structure. For wavelengths shorter than about 1 μ, effects are seen which can be attributed to a photoemission of electrons from the InSb into the oxide. Some of the photoemitted electrons are trapped in the oxide, creating an electric field which modifies the extent of the depletion region in the InSb. At very short wavelengths the light is absorbed in the oxide causing it to become conductive, which allows some of the trapped electrons to escape causing a corresponding modification of the InSb depletion region. The spectral data of the accompanying figures will be discussed in terms of these mechanisms.

We referred above to a depletion region in the n-type InSb at the oxide-InSb interface. However, n-type InSb unbiased structures cooled to 77°K while in the dark, do not exhibit a depletion region. The data indicates that an n-type accumulation region forms under these conditions. The energy diagram depicting this situation is given in Fig. I-11(a). Upon exposure to ordinary room lights or controlled radiation of wavelengths shorter than about 1 μ, a depletion region forms as shown in Fig. I-11(b) because of the induced charge transfer. If p-type InSb is used to fabricate the structure and it is cooled in the dark, a depletion region is obtained as shown in Fig. I-11(c). With short wavelength radiation this region can be eliminated, resulting in the situation depicted in Fig. I-11(d). The change in the InSb depletion regions between Figs. I-11(a) and (b) and between Figs. I-11(c) and (d) can also be accomplished by applying DC voltages to the structure. A depletion region modified by radiation can thus be forced back toward its initial state by the application of a bias.

At room temperatures we cannot detect a depletion region in the InSb because of the large number of thermally generated carriers; however, we are able to observe the photoemission from the InSb into the oxide and the photoconductivity of the oxide. Unnormalized spectra at different applied bias voltages are shown in Fig. I-12. A positive voltage corresponds to the potential of the metal surface relative to the grounded InSb side. The large intensity variations of the Xenon lamp and monochromator used as a source for these studies are also shown. The curves of Fig. I-12 show that the photoemission is observed down to about 1.2 eV. The signal at high photon energies is associated with the photoconductivity of the oxide and is observed to change sign with bias. However, the lower energy response due to photoemission from the InSb gives only the one polarity. This polarity is that which would arise due to emission of electrons from the InSb into the oxide.

Measurements similar to those shown in Fig. I-12 were also taken at 77°K and the DC photoresponse yielded essentially the same spectra. A change in signal amplitudes was obtained which could be correlated with the increased resistance of the oxide. Samples prepared from p-type and n-type InSb gave essentially the same spectral results except, again, for variations in magnitude.

To measure more directly the "writing" and "erasing" photon energies, we used the modulated 3.9-μ emission from an InAs diode source to determine the condition of the depletion region. With no depletion region, no signal as a result of the 3.9 μ source is obtained, but as the depletion region builds up, the response increases correspondingly. The results are shown in Fig. I-13 for n-type InSb devices. Each point of the spectra was obtained by exposing the structure to photons of the energy indicated, turning off this radiation and then measuring the response

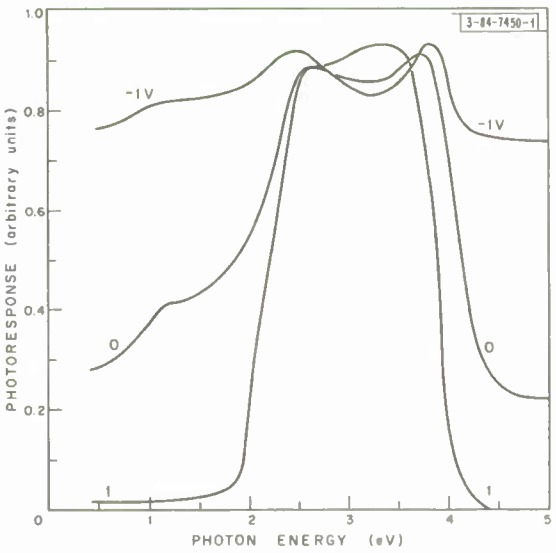

Fig. I-13. Photoresponse to moduloted 3.9-μ InAs diode rodiatian (in orbitrary units) versus photon energy for n-type InSb-MOS device, with different opplied biases at 77°K. Applied bioses ore indicoted on curves.

to the InAs 3.9-μ radiation. As indicated, biases were also applied which were left on during the exposure intervals and whilc probing with the 3.9-μ light. The most dramatic changes in both n- and p-type devices were obtained with +1V bias applied to the Ni layer. For the n-type samples of Fig. I-13 a bias of +1V tends to decrease the depletion region but with exposure to photons in the energy interval of 2 to 4 eV thc photoemission and consequent trapping of charge produces a field greater than that of the applied bias. At the ultraviolet end of the spectrum, thc charge is released and thc depletion region is again eliminated. A complementary behavior is expected and obtained for the p-type samples.

W. E. Krag
R. J. Phelan, Jr.
J. O. Dimmock

G. TEMPERATURE AND COMPOSITIONAL DEPENDENCE OF LASER EMISSION IN $Pb_{1-x}Sn_xSe$

We have observed laser emission from diodes fabricated from the semiconducting pseudobinary alloy $Pb_{1-x}Sn_xSe$ in the composition range $0 \leqslant x \leqslant 0.276$ and havc studied the energy of laser emission as a function of composition and temperature. Previously, laser action[31,32] was observed in p-n junctions of $Pb_{1-x}Sn_xSe$ for x up to 0.08. The results of these studies strongly support the model[33] in which the valence and conduction bands invert and exchange roles in thc $Pb_{1-x}Sn_xSe$ alloy serics as x is increased from zero to 0.4. This model was originally proposed to explain the composition and temperature dependence of the energy gap in the $Pb_{1-x}Sn_xTe$ alloys and it was at that time suggested that the same model should apply to the $Pb_{1-x}Sn_xSc$ alloys as wcll. Although previous workers[31,34] have obtained strong cvidence that the band inversion model is applicable in the $Pb_{1-x}Sn_xSe$ alloys it is felt that the new results presented here confirm the model rather conclusively. In addition, we havc now observed laser emission throughout the wavelength range from 8 to 31.2 μ. The observation of laser emission

for various compositions provides strong evidence for a direct energy gap for all compositions of $Pb_{1-x}Sn_xSe$ in the range x = 0 to x = 0.276.

In this study, crystals were grown from the vapor using the type of growth ampoule described previously.[35] After a growing time of about 20 hours using a source powder of $(Pb\text{-}Sn)_{0.51}Se_{0.49}$, the vapor-grown crystals were furnace-cooled to 625°C from the growth temperature of 800°C, isothermally annealed at 625°C for 72 hours and quenched in water. In the same sealed ampoule, the crystals were slowly heated to 425°C, isothermally annealed for 1 hour at 425°C, and furnace cooled to room temperature. The crystals were transferred to a second ampoule containing powder of composition $(Pb\text{-}Sn)_{0.49}Se_{0.51}$ and carried through the above 425°C process again. During the latter process, a thin surface layer of the n-type crystal is converted to p-type. The crystals were cleaved, gold plated, indium plated and mounted in low inductance packages using In-Ga solder to bond the indium plate to the current leads. The diodes were then mounted in a commercial, variable temperature dewar and the laser emission energy and laser threshold current were measured by standard techniques as the temperature was varied. Experimental results for three laser diodes of $Pb_{1-x}Sn_xSe$ with x = 0.19, x = 0.218 and x = 0.276 are displayed graphically in Fig. I-14 and given in Table I-2.

The emission energy was observed to decrease as the temperature was increased, as shown in Fig. I-14, and the laser threshold current increased slowly. However, as the temperature approached a value corresponding to a reduced laser emission energy of approximately 8 kT (see Table I-2), the threshold energy increased sharply and finally the diode stopped lasing. The temperature cutoff, temperature coefficient of the laser emission energy, and reduced emission energy of three inverted gap materials are shown in Table I-2. The data indicate that the temperature coefficient increases somewhat as the SnSe content increases from x = 0.218 to x = 0.276.

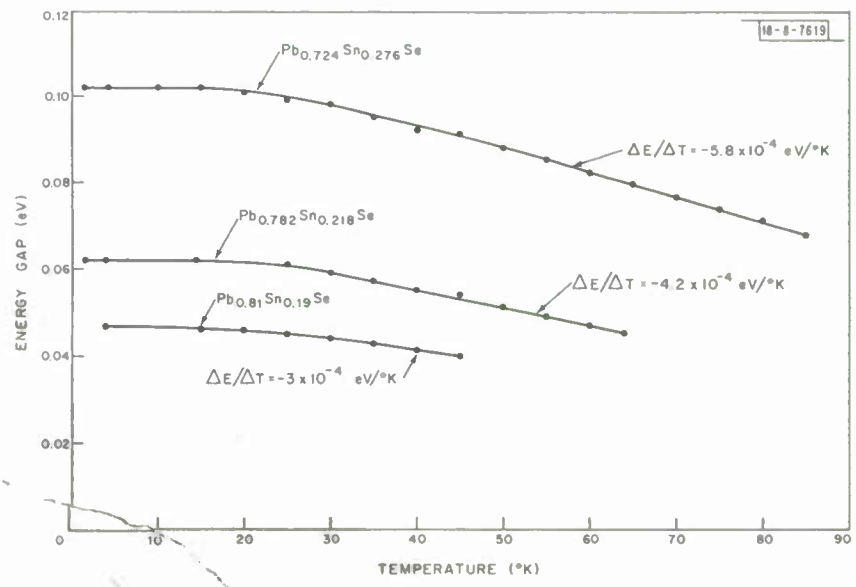

Fig. I-14. Plot of variation of laser emission energy with temperature for three $Pb_{1-x}Sn_xSe$ diode lasers with x = 0.276, 0.218 and 0.19.

TABLE I-2

TEMPERATURE COEFFICIENT OF LASER EMISSION ENERGY, $\Delta E/\Delta T$, LASER EMISSION ENERGY AT THE TEMPERATURE OF CUTOFF E_t, TEMPERATURE OF CUTOFF T_t, AND E_t/kT_t

Mole Fraction of SnSe, x	$\Delta E/\Delta T$ eV/°K	E_t(eV)	T_t	E_t/kT_t
0.276 ± 0.008	-5.8×10^{-4}	0.0675	85°K	9.2
0.218 ± 0.002	-4.2×10^{-4}	0.0450	64°K	8.2
0.190 ± 0.004	-3×10^{-4}	0.0398	45°K	10

At low temperatures, the coefficient decreases to a very small value for not only these compositions but also for PbSe. Above about 30°K, the temperature dependence of the energy gap is approximately $+4 \times 10^{-4}$eV/°K for PbSe, opposite in sign to that of the alloys studied here. A change in sign in the temperature coefficient of the laser emission is consistent with the inverted energy gap model.[33] Also, Table I-2 shows the compositional dependence of the energy gap as determined at 12°K for various lasers of $Pb_{1-x}Sn_xSe$. The various compositions were determined by electron beam microprobe analysis and the probable compositional error range is indicated in the table. Since the compositional dependence of E_G for high Sn contents is opposite in sign to those for low Sn contents, additional evidence is provided for the inverted model.

T. C. Harman I. Melngailis
A. R. Calawa J. O. Dimmock

H. MAGNETIC FIELD DEPENDENCE OF LASER EMISSION IN $Pb_{1-x}Sn_xSe$ DIODES

We have measured the laser emission energy as a function of magnetic field up to 50 kG in a number of $Pb_{1-x}Sn_xSe$ diodes in the composition range $0 \leqslant x \leqslant 0.276$. For the first time in any material to our knowledge, the emission energy of the lowest energy line has been found to decrease as the magnetic field strength is increased. This occurs in the case of the higher Sn content alloys with $x \geqslant 0.19$. Thus, these results suggest that it may be possible to tune the laser emission energy to very long wavelengths using a magnetic field.

For these experiments the diodes were mounted in the core of a solenoidal superconducting magnet and were oriented with the current parallel to the magnetic field, both being along a [100] crystallographic direction. The radiation is emitted perpendicular to this direction along another [100] crystallographic axis. Spectra were obtained as a function of magnetic field and the energies of the laser emission peaks are shown for a typical diode with high Sn content in Fig. I-15. At low and intermediate current levels, a single emission peak is observed whose energy increases rapidly with increasing magnetic field. However, at an intermediate value of magnetic field the emission switches to a lower energy peak whose energy decreases with further

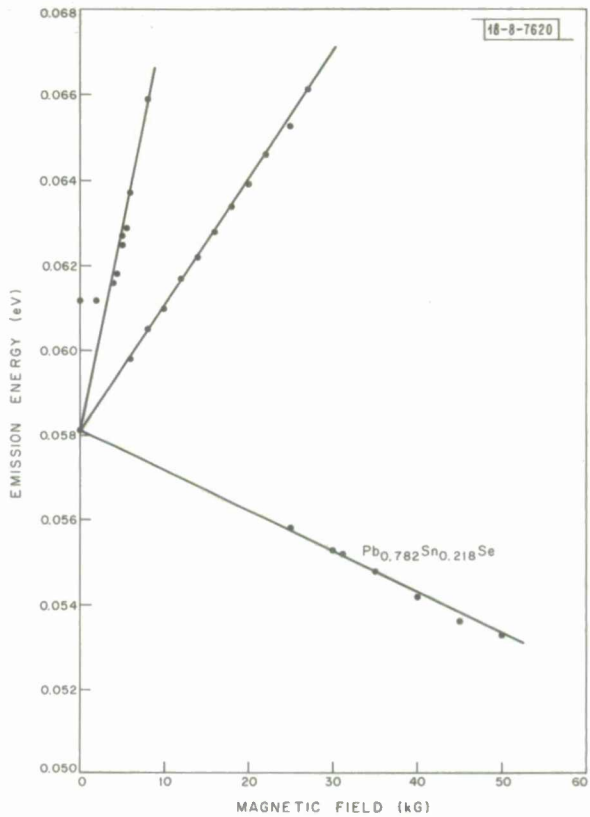

Fig. I-15. Energy of diode laser emission versus magnetic field.

increase in field. A third higher lying emission line is observed by using high current pulses. The observed emission peaks have energies which are a linear function of magnetic field and represent transitions between various conduction and valence band magnetic levels.

The decrease in the energy of the lowest emission line as the magnetic field increases is readily understandable on the basis of the inverted band model for the $Pb_{1-x}Sn_xSe$ alloys with higher Sn content.[33] Consider a simple two band model in which the effective mass tensor and g-factors of the conduction band are determined solely by the presence of a valence band, separated from it by a small energy gap, and vice versa. If the interaction with all other energy bands is neglected Cohen and Blount[36] have shown that there is a relationship between the effective masses and g-factors such that the lowest conduction band and highest valence band Landau level with n = 0 and spin = −1 should each have an energy which is independent of magnetic field.

Baraff[37] has considered an extension of this model in which the interaction with other energy bands is considered in second order perturbation theory. This results in a small field dependence of the n = 0 and spin = −1 conduction and valence band Landau levels, which is given by

$$E_1 = E_g + (\tfrac{1}{2}\,A\text{-}B)\,H \qquad (I\text{-}1)$$

and

$$E_2 = +(\tfrac{1}{2}\ C\text{-}D)\ H \qquad (I\text{-}2)$$

where, if the subscript 1 refers to the conduction band (L_6^- in PbSe), and 2 refers to the valence band (L_6^+ in PbSe), A and C represent a deviation in the L_6^- and L_6^+ effective masses, respectively, and B and D represent a deviation in the L_6^- and L_6^+ g-factors, respectively, from the values predicted by the two band model, all due to interactions with other bands.

The magnetic field dependence of the longest wavelength laser emission in PbSe for H parallel to [100] is about $+1.0 \times 10^{-7}$eV/Gauss which corresponds to $\frac{1}{2}(A\text{-}C) - (B\text{-}D)$ in the theory of Baraff. In our model[33] for the energy bands in the PbSnSe alloys the valence and conduction bands in the higher Sn alloys are inverted from those in PbSe. That is, L_6^+ becomes the conduction band and L_6^- becomes the valence band. Neglecting any other changes, Eqs. (I-1) and (I-2) become in this case

$$E_1 = E_g + (\tfrac{1}{2}\ C\text{-}D)\ H \qquad (I\text{-}3)$$

and

$$E_2 = +(\tfrac{1}{2}\ A\text{-}B)\ H \qquad (I\text{-}4)$$

and the magnetic field dependence of the longest wavelength laser emission in these alloys should be given by $\frac{1}{2}(C\text{-}A) - (D\text{-}B)$ which is just the negative of the field dependence in PbSe. The values of -0.9×10^{-7}eV/Gauss for an alloy with x = 0.218, and -1.1×10^{-7}eV/Gauss for an alloy with x = 0.276, are in good agreement with this model. This lends additional support to the model that the energy bands in PbSnSe cross over with increasing Sn concentration. It should be noted in conclusion that according to the theory of Baraff there are higher order matrix elements which prevent these two lowest levels from crossing but that the minimum separation distance should be quite small, of the order of 10^{-4}eV at 100 kG.

A. R. Calawa T. C. Harman
J. O. Dimmock I. Melngailis

I. INTERDIFFUSION IN PbSe

Interdiffusion in PbSe has been described by Fick's law using two diffusion constants, one for the diffusion of excess Pb into PbSe and the other for the diffusion of excess Se into PbSe.[38] By measuring the motion of a p-n junction in PbSe as a function of time and temperature, it was found that the diffusion coefficient for diffusing from an excess selenium vapor in lead-saturated PbSe is about nine times larger than that for diffusing from an excess lead vapor into selenium saturated material. This suggested that the diffusion coefficient for this interdiffusion process may be dependent on the relative concentrations of the interdiffusing species. In an attempt to determine this dependence several diffusions were performed using materials of different initial concentrations, Δ_o, but keeping the surface concentration, Δ_s, constant. Some preliminary results are shown in Fig. I-16. The upper points are diffusion coefficients for the diffusion of Se into Pb-rich PbSe substrates. The lower points are diffusion coefficients for the diffusion of Pb into Se-rich PbSe. The diffusion coefficient in each case was calculated assuming a Fick's

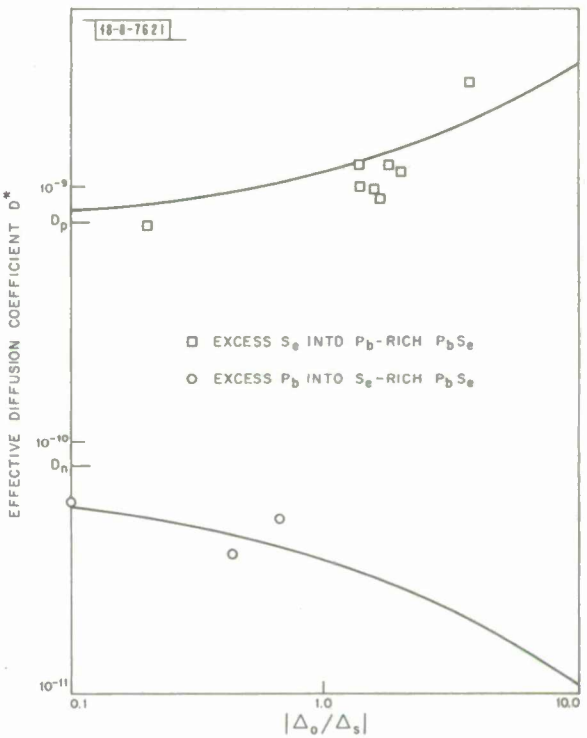

Fig. I-16. Concentration dependence of effective diffusion coefficient for p-n junction movement in PbSe at 400°C. Solid lines are theoretical curves for $D_p/D_n = 9$.

law dependence and a diffusion from a constant surface concentration into a semi-infinite solid. The results show that the diffusion coefficient varies with initial concentration of the PbSe substrate.

This data is in essential agreement with a diffusion model[39,40] which assumes that the interdiffusion coefficient has two values, D_p in Se-rich material and D_n in Pb-rich material with $D_p = 9\,D_n$. D_p and D_n are assumed to be constant and change abruptly from one value to the other at the p-n junction. The concentration profiles on both sides of the junction are obtained by solving Fick's equation using constant diffusion coefficients and maintaining continuity of concentration and diffusion current at the junction.

It was found that the rate of junction movement could be described by an effective diffusion coefficient D* which depends on the ratio of initial concentration to surface concentration Δ_o/Δ_s. The solid lines in Fig. I-16 are a best fit of D* to the currently available data. The agreement seems promising and efforts are under way to obtain more experimental points.

R. W. Brodersen†
J. N. Walpole†
A. R. Calawa

† Author not at Lincoln Laboratory.

REFERENCES

1. K.M. Johnson, IEEE Trans. Electron Devices ED-12, 55 (1965).
2. M.P. Lepselter and S.M. Sze, Bell System Tech. J. 47, 195 (1968).
3. C.M. Wolfe and W.T. Lindley, J. Electrochem. Soc. 116, 276 (1969).
4. A.G. Foyt, W.T. Lindley, J.P. Donnelly, and C.M. Wolfe, Solid State Electron. (to be published).
5. C.N. Potter and D.E. Sawyer, Rev. Sci. Instr. 39, 180 (1968).
6. H. Melchior and W.T. Lynch, IEEE Trans. Electron Devices ED-13, 829 (1966).
7. H. Melchior and L.K. Anderson, International Electron Devices Meeting, Washington, D.C. (1965).
8. R.D. Baertsch, IEEE Trans. Electron Devices ED-13, 383 (1966).
9. R.J. McIntyre, IEEE Trans. Electron Devices ED-13, 164 (1966).
10. S.L. Miller, Phys. Rev. 99, 1234 (1955).
11. C.A. Lee, R.A. Logan, R.L. Batdorf, J.J. Kleimack, and W. Wiegmann, Phys. Rev. 134, A761 (1964).
12. R.A. Logan and S.M. Sze, J. Phys. Soc. Japan 21, Supplement, 434 (1966).
13. C. Penchina, A. Frova, and P. Handler, Bull. Am. Phys. Soc. 9, 714 (1964).
14. L.J. Van der Pauw, Phillips Res. Repts. 13, 1 (1958).
15. C.O. Thomas, D. Kahng, and R.C. Manz, J. Electrochem. Soc. 109, 1055 (1962).
16. W.E. Taylor, N.H. Odell and H.Y. Fan, Phys. Rev. 88, 867 (1952).
17. L. Sosnowski, J. Phys. Chem. Sol. 8, 142 (1959).
18. H.F. Matâre, J. Appl. Phys. 30, 581 (1959).
19. W.T. Read, Phil. Mag. 45, 775 (1954).
20. J.R. Knight, D. Effer and P.R. Evans, Solid State Electron. 8, 178 (1965).
21. D. Effer, J. Electrochem. Soc. 112, 1020 (1965).
22. E.W. Mehal and G.R. Cronin, Electrochem. Tech. 4, 540 (1966).
23. C.M. Wolfe, T.M. Quist and A.J. Strauss, Solid State Research Report, Lincoln Laboratory, M.I.T. (1966:2), p. 7, DDC 639064.
24. J. Whitaker and D.E. Bolger, Solid State Commun. 4, 181 (1966); D.E. Bolger, J. Franks, J. Gordon and J. Whitaker, Proc. Intern. Symp. Gallium Arsenide, Reading, 1966 (Institute of Physics and The Physical Society, London), p. 16 (1967).
25. C.S. Kang and P.E. Greene, Appl. Phys. Letters 11, 171 (1967).
26. E. Andre and J.M. LeDuc, Mat. Res. Bull. 3, 1 (1968).
27. C.M. Wolfe, A.G. Foyt and W.T. Lindley, Electrochem. Tech. 6, 208 (1968), DDC 673592.
28. R.J. Phelan, Jr. and J.O. Dimmock, Appl. Phys. Letters 11, 359 (1967), DDC 669211.
29. W.E. Krag, R.J. Phelan, Jr. and J.O. Dimmock, Solid State Research Report, Lincoln Laboratory, M.I.T. (1968:3), p. 7, DDC 678534.
30. R.J. Phelan, Jr. and J.O. Dimmock, Appl. Phys. Letters 10, 55 (1967), DDC 653365.
31. J.F. Butler, A.R. Calawa, and T.C. Harman, Appl. Phys. Letters 9, 427 (1966), DDC 653367.
32. J.F. Butler and T.C. Harman, IEEE Solid-State Device Research Conf., Santa Barbara, Calif., 19-21 June 1967.

33. J.O. Dimmock, I. Melngailis and A.J. Strauss, Phys. Rev. Letters 16, 1193 (1966), DDC 642225.

34. A.J. Strauss, Phys. Rev. 157, 608 (1967).

35. J.F. Butler and T.C. Harman, Appl. Phys. Letters 12, 347 (1968), DDC 673601.

36. M.H. Cohen and E.I. Blount, Phil. Mag. 5, 115 (1960).

37. G.A. Baraff, Phys. Rev. 137, A842 (1965).

38. A.R. Calawa, T.C. Harman, M.C. Finn and P. Youtz, Trans. Met. Soc. AIME 242, 374 (1968), DDC 678986.

39. R.W. Brodersen, "Concentration Dependent Interdiffusion in the Lead Chalcogenides," Master's Thesis, Department of Electrical Engineering, M.I.T., 1968.

40. R.W. Brodersen, J.N. Walpole, and A.R. Calawa, Meeting of the Electrochemical Society, Montreal, October, 1968.

II. MATERIALS RESEARCH

A. TRANSPARENT FURNACE FOR VAPOR CRYSTAL GROWTH

Since the growth of large crystals from the vapor phase requires rather long periods, it would be extremely advantageous to be able to monitor the process visually in order to modify the growth conditions or to terminate the experiment in case of failure. This is quite difficult to accomplish with a resistance-heated furnace insulated by asbestos or similar opaque material, since a viewing port is generally cooled sufficiently by radiation loss to become obscured by condensation of the vapor.

To solve this problem, we have developed a transparent, resistance-heated tube furnace for operation at temperatures up to 1000° to 1100°C. In this furnace conventional insulation is entirely replaced by a layer of gold, about 400 Å thick, deposited on Pyrex. Such a layer is an effective insulator because of its very high reflectivity in the infrared beyond 1 μm, where a blackbody emits 99.8 percent of its energy at 1000°C and 99 percent of its energy at 2000°C, but it is thin enough to be quite transparent in the visible (see Fig. II-1). Metal reflectors have been employed previously to insulate furnaces,[1,2] but the use of transparent films for this purpose has not been reported. Although many metals are highly reflecting in the infrared, only a few transmit sufficiently in the visible to be transparent, and of these gold is the most suitable for furnace construction because of its inertness.

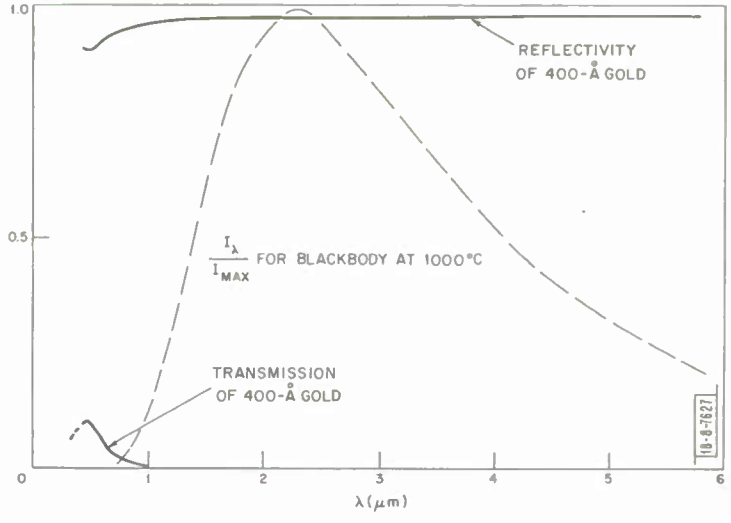

Fig. II-1. Transmission and reflectivity of gold layer 400 Å thick, and relative energy distribution of 1000°C blackbody.

Several different versions of the transparent furnace have been constructed. Each consists of three concentric parts, an inner silica tube in which crystal growth occurs, a heating element, and an outer Pyrex tube with the gold layer deposited on its inner surface. One convenient type

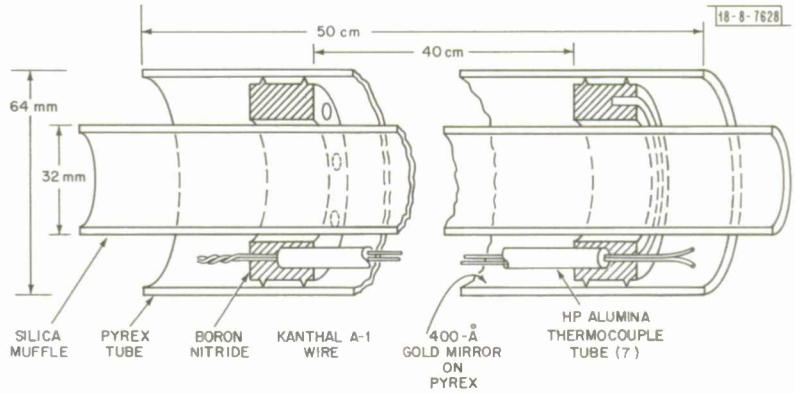

Fig. II-2. Canstructian drawing af transparent furnoce.

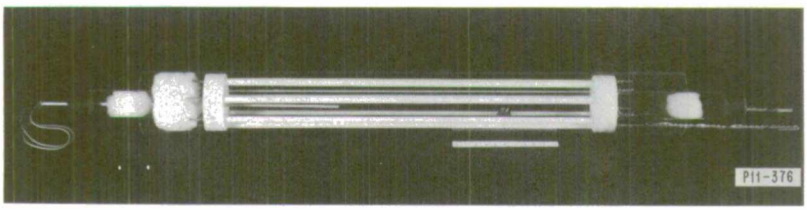

Fig. II-3. Photograph of transparent furnoce showing os-grown ZnTe crystol.

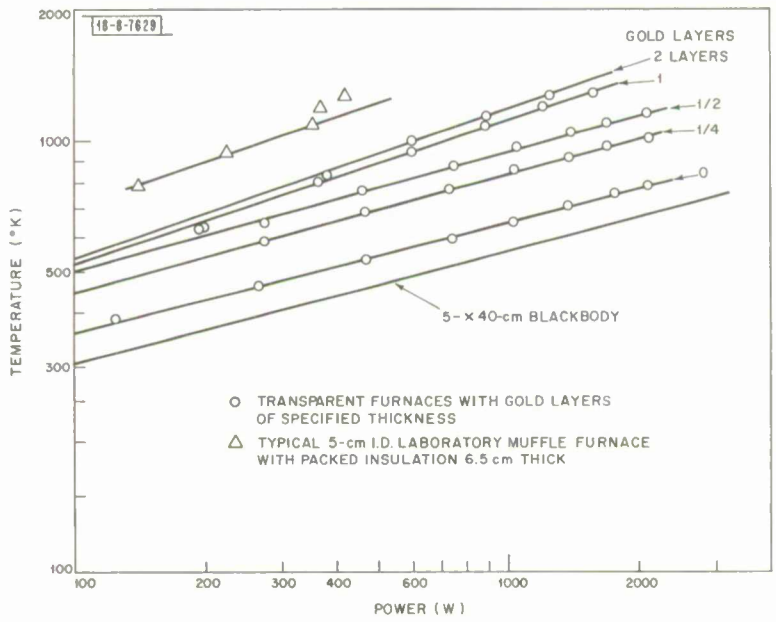

Fig. II-4. Temperoture os o function of input power for voriaus furnoces. The power rodioted by a blockbody, 5 cm diameter by 40 cm long, is shown for reference.

is shown schematically in Fig. II-2. Figure II-3 is a photograph of this furnace, which uses a cage type heating element consisting of seven two-hole thermocouple protection tubes (1/4 in. diameter, 99 percent alumina) suspended by boron nitride end rings. The tubes hold 6 m of 16 ga. Kanthal A-1 wire with a cold resistance of 6.2 ohm and a thermal loading of 39 watts/in.^{2} This furnace can be operated in either the vertical or horizontal position; another type of heating element in which the heater wire was wound in a spiral on quartz was satisfactory for horizontal but not for vertical operation.

The gold mirrors have been prepared by two different methods. The first type was made by electroplating a long tungsten wire with gold, hanging the wire along the axis of the Pyrex tube inside a vacuum bell jar, and depositing the gold by evaporation. These mirrors were moderately adherent and in some cases could be used for many days, but they could easily be scratched when the heating element was inserted and sometimes deteriorated after only a few days of operation.

More satisfactory gold layers have been prepared by decomposition of a commercial gold resinate solution. After the Pyrex tube is scrubbed in hot Alconox, one end is stoppered and a small amount of solution poured in. The inside is evenly coated with solution by rolling the tube almost horizontally, gradually erecting the tube to leave a uniform layer of liquid, removing the stopper, and draining off the excess. The tube is immediately fired by passing it at 1 cm/min through a furnace maintained at about 600°C, while air is gently blown through from the resin side. After the organic resin is burnt off, the tube is annealed at 600°C overnight to increase the adhesion. These chemically deposited mirrors, while not quite as uniform as the vacuum deposited mirrors, are extremely adherent. They can be made thinner by diluting the solution with spraying medium #7874.

In order to determine the effectiveness of the gold insulation as a function of thickness, Pyrex tubes were coated by chemical deposition with gold films nominally 2, 1, 1/2, and 1/4 layers thick. (The 2-layer film was obtained by successive depositions with full strength solution, while the fractional layers were prepared with appropriately diluted solutions.) The temperatures attained in the furnace of Fig. II-3 by using these tubes are shown as a function of input power in Fig. II-4, together with similar plots for the same furnace with an uncoated Pyrex tube, and for a typical 5-cm i.d. laboratory muffle furnace with conventional packed insulation 6.5-cm thick. The temperature attained with a fixed input power increases with increasing film thickness, but there is little increase in temperature when a 1-layer film is replaced by a 2-layer film. It is seen that the input power for each individual furnace increases with very nearly a T^4 dependence.

The transparent furnace shown in Fig. II-3 has been used successfully for a number of vapor growth experiments on ZnTe. The single crystal shown in the photograph, which is 1.7 cm in its longest dimension, was grown in 48 hours.

T. B. Reed

B. GROWTH OF $RbNiF_3$ SINGLE CRYSTALS

Because $RbNiF_3$ is a transparent ferrimagnet with large optical Faraday rotation,[3] it is of considerable interest for a variety of magneto-optical experiments. We have developed a method

for growing $RbNiF_3$ single crystals of sufficient size (1 cm diameter, 5 cm long) and optical quality for such experiments.[4] It should be possible to use essentially the same method for growing single crystals of other ABF_3 compounds.

Small stoichiometric crystals of $RbNiF_3$ are first prepared[5] by the double decomposition of RbF and $NiCl_2$ in a Pt crucible at 1000°C under dry argon. About 10 percent by weight of NH_4HF_2 is added to the compound. The mixture is dried by conventional techniques and then placed in the growth apparatus shown schematically in Fig. II-5. This apparatus consists of a monel headpiece sealed by a water-cooled Teflon gasket to an inconel tailpiece, inside which a graphite crucible is mounted on a nickel rod. The headpiece is provided with a gas inlet, a gas outlet, and a connection to a high vacuum manifold. Graphite is used as the crucible material because it is inert and is not wet by molten fluorides, so that grown crystals can easily be removed from a tapered crucible. The Ni rod provides good heat flow from the crucible.

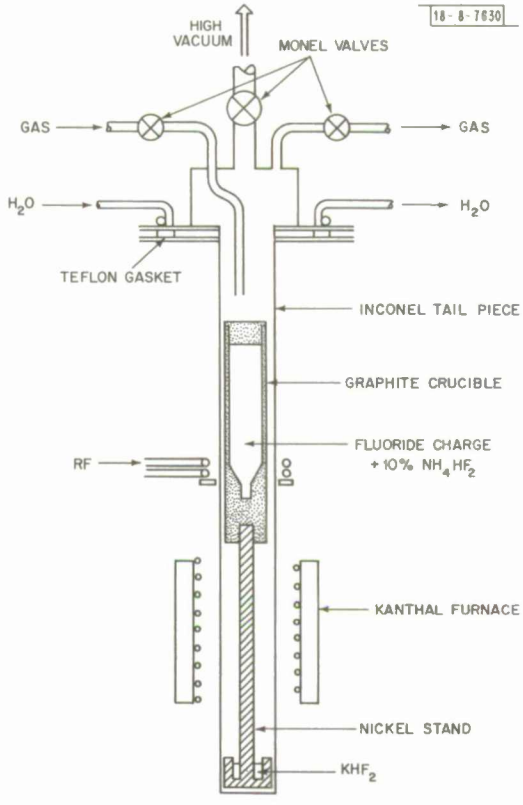

Fig. II-5. Apparatus for growing single crystals of $RbNiF_3$ and other ABF_3 crystals.

Many fluorides hydrolyze at low temperatures. In order to remove as much adsorbed water as possible, the apparatus is alternately evacuated and flushed with dry argon. It is then lowered so that the crucible is positioned within the Kanthal resistance furnace. The system is evacuated and maintained at a pressure of less than 10^{-6} torr while the furnace is slowly heated to 100°C to remove water vapor. The vacuum valve is closed, and argon is allowed to flow through the system. The temperature is then raised to 300°C. At about 200°C the NH_4HF_2 decomposes, yielding HF which removes contaminants from the $RbNiF_3$ charge. After the decomposition is complete, the gas inlet and outlet valves are both closed. Power to the resistance furnace is then increased to heat the charge to about 200°C above its melting point (T_M = 960°C for $RbNiF_3$). This process reduces the viscosity of the melt sufficiently to permit any trapped gas bubbles to escape.

The power to the resistance furnace is now reduced. The apparatus is pressurized with argon at about 1 atm, in order to prevent decomposition of the charge during crystal growth, and then raised until the bottom of the crucible is just above the RF coil. A partial pressure of HF is supplied by heating the bottom of the tailpiece to 200°C in order to decompose a quantity of KHF_2 located there. The temperature of the Kanthal resistance furnace is raised to about 200°C below the melting point of the charge. Sufficient power is supplied to the RF coil to melt a small layer of the charge, and crystal growth proceeds as the apparatus is lowered through the coil.

Use of RF heating makes it possible to achieve high temperature gradients (~200°C/cm) and therefore to use reasonable growth rates (~1 cm/h) without encountering difficulties caused by undercooling. RF heating is also advantageous because only a small portion of the charge is molten at any one time; this reduces the loss of fluorine and also the contamination of the melt by the apparatus.

J. R. O'Connor
L. J. Small
A. R. Leyenaar

C. EFFECT OF PRESSURE AND B-CATION SIZE ON CRYSTAL STRUCTURE OF $CsBF_3$ COMPOUNDS

At atmospheric pressure, each of the compounds $CsBF_3$ (B = Mn, Fe, Co, Ni, Cd) exists in one of four related close packed structures that have been described earlier.[6] For $CsNiF_3$, which has the smallest B cation, the structure has only hexagonal close packed CsF_3 layers with all NiF_6 octahedra face shared, giving a $\underline{c}$ axis repeat of two layers (2L). As the B cation size increases, so does the proportion of cubic close packing. For $CsCoF_3$, 1/3 of the layers are cubic close packed leading to a nine layer stacking sequence (9L). For $CsFeF_3$ and $CsMnF_3$, 2/3 of the layers are cubic close packed and there is a six layer stacking sequence (6L). Finally, $CsCdF_3$ has only cubic close packed layers with all octahedra corner shared, giving the perovskite structure.

We have found that high pressure treatment of the $CsBF_3$ compounds at elevated temperatures results in a number of transformations involving an increase in the ratio of cubic to hexagonal close packed layers. Details of sample preparation and high pressure treatment have been given earlier.[7] The high pressure phases were retained by quenching from 700°C to room temperature before reducing the pressure, and then identified by powder X-ray diffraction. These retained phases require heating for a few hours at 200° to 500°C for retransformation to their atmospheric pressure forms (APF). In each pressure induced transformation, the initial structure is changed into the next higher one in the sequence 2L → 9L → 6L → perovskite. The 2L structure (APF) of $CsNiF_3$ transforms to the 9L at 5 kbars and then to the 6L at 47 kbars.[7] The 9L (APF) $CsCoF_3$ transforms at 22 kbars to the 6L. For $CsFeF_3$, the 6L (APF) transforms at about 70 kbars to the perovskite, while the 6L (APF) $CsMnF_3$ requires only 26 kbars for the same transformation. These transformations are summarized in Fig. II-6, where the observed structures are shown on a plot of pressure vs ionic radius of the B cation. Each B cation radius was calculated by subtracting the ionic radius of F^{-1} in two-fold coordination[8] from one-half the unit cell dimension of the KBF_3 perovskite. The radii obtained in this way are consistent with the volumes of the BF_2 rutiles and of the $CsBF_3$ compounds we have investigated. The cell

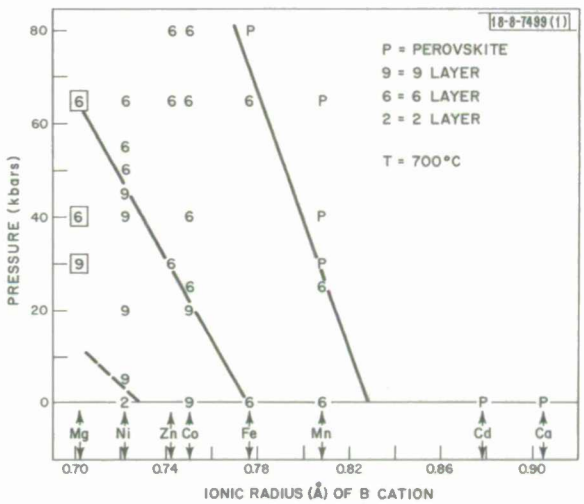

Fig. II-6. Effect of pressure and B-cation size on crystal structure of $CsBF_3$ compounds.

TABLE II-1
UNIT CELL DIMENSION (Å) AND VOLUME PER MOLECULE ($Å^3$) FOR $CsBF_3$ COMPOUNDS

Compound	Units	Structure Type			
		2L (hexagonal)	9L (hexagonal)	6L (hexagonal)	Perovskite (cubic)
$CsNiF_3$	Å	6.24 × 5.22	6.15 × 22.32	6.05 × 14.55	
	$Å^3$	88.0	81.2	76.9	
$CsCoF_3$	Å		6.20 × 22.36	6.09 × 14.67	
	$Å^3$		82.7	78.5	
$CsFeF_3$	Å			6.16 × 14.86	4.283
	$Å^3$			81.3	78.6
$CsMnF_3$	Å			6.213 × 15.074	4.328
	$Å^3$			84.0	81.1
$CsMgF_3$	Å		6.16 × 22.13	6.04 × 14.45	
	$Å^3$		80.8	76.1	
$CsZnF_3$	Å			6.09 × 14.67	
	$Å^3$			78.5	

TABLE II-2
VOLUME DECREASE (%) DUE TO PRESSURE-INDUCED TRANSFORMATIONS OF $CsBF_3$ COMPOUNDS

Transformation	B-Cation				
	Ni	Co	Fe	Mn	Mg
2L → 9L	7.7				
9L → 6L	5.3	5.1			5.8
6L → Perovskite			3.3	3.4	

dimensions and volumes of the latter are given in Table II-1. Each of the high pressure transformations involves a sizeable volume decrease, as tabulated in Table II-2. The percentage change in volume is shown to decrease as the proportion of cubic close packing increases.

For $CsZnF_3$ and $CsMgF_3$, no stable atmospheric pressure phase is formed. However, $CsZnF_3$ forms the 6L structure at pressures greater than 30 kbars. $CsMgF_3$ has the 9L structure at 30 kbars and is transformed into the 6L structure between 30 and 40 kbars. The pressure for the 9L → 6L transformation is much too low to be consistent with the phase diagram drawn in Fig. II-6. This inconsistency indicates that the field of stability for these structures is not determined solely by geometric considerations. Both Mg and Zn are quite different from the other B cations studied. Unlike the transition metals Mn, Fe, Co, and Ni, neither Mg nor Zn has any unpaired electrons, and they are more basic and ionic than the other elements. These characteristics are expected to inhibit the tendency of Mg and Zn to occupy face-shared octahedra and therefore to lower the pressures required to effect transformations to structures with more cubic close packing.

J. M. Longo D. A. Batson
J. A. Kafalas T. W. Hilton

D. HOMOGENEITY RANGE AND PARTIAL PRESSURES OVER Bi_2Te_3(c)

Although the semiconducting compound Bi_2Te_3 has been the subject of a number of investigations in recent years, there are important gaps in our knowledge of this material. The only vapor pressure measurements have been Knudsen cell weight-loss measurements[9,10] which give no direct indication of the vapor species involved nor of the variation of partial pressures along the three-phase curve of Bi_2Te_3. There has been only one partially successful attempt,[11] based on precision density measurements, to check the correctness of the antistructure defect model suggested[12] on the basis of Hall coefficient measurements on the first-to-freeze crystals from melts of known composition. Moreover there has been no detailed, direct determination of the homogeneity range.

We have filled these gaps by determining the partial pressure of Te_2 as a function of temperature for a number of pre-annealed Bi-Te compositions between 44 and 70 atomic percent Te. The technique used was that of measuring the optical density of the coexisting vapor phase as a function of wavelength by using a Cary 14-H double-beam spectrophotometer. We have previously applied this technique to a number of telluride and selenide systems as well as to Te (Ref. 13) and Se themselves. In the present investigation the Te_2 partial pressure, p_{Te_2}, was obtained primarily from the absorption near 2000 Å, which is about 10 times stronger than that near 4357 Å. The results are shown in Fig. II-7, where p_{Te_2} is plotted against $10^3/T$ for various compositions. The large parabola-like curve gives the values of p_{Te_2} along the three-phase curve of Bi_2Te_3 (i.e., along the solidus lines of Bi_2Te_3). Since values of p_{Te_2} for the 60.07, 59.99, 59.90, and 59.80 atomic percent Te compositions fall within this three-phase curve, these compositions lie within the Bi_2Te_3 homogeneity range. The straight lines to the left of the three-phase curve give p_{Te_2} as a function of $10^3/T$ for melts of various compositions. The liquidus line constructed from these data agrees to within 1 °C with liquidus points recently determined in our Laboratory by differential thermal analysis. The data points for the two compositions represented by +, and the two compositions represented by X, do not overlap. Hence,

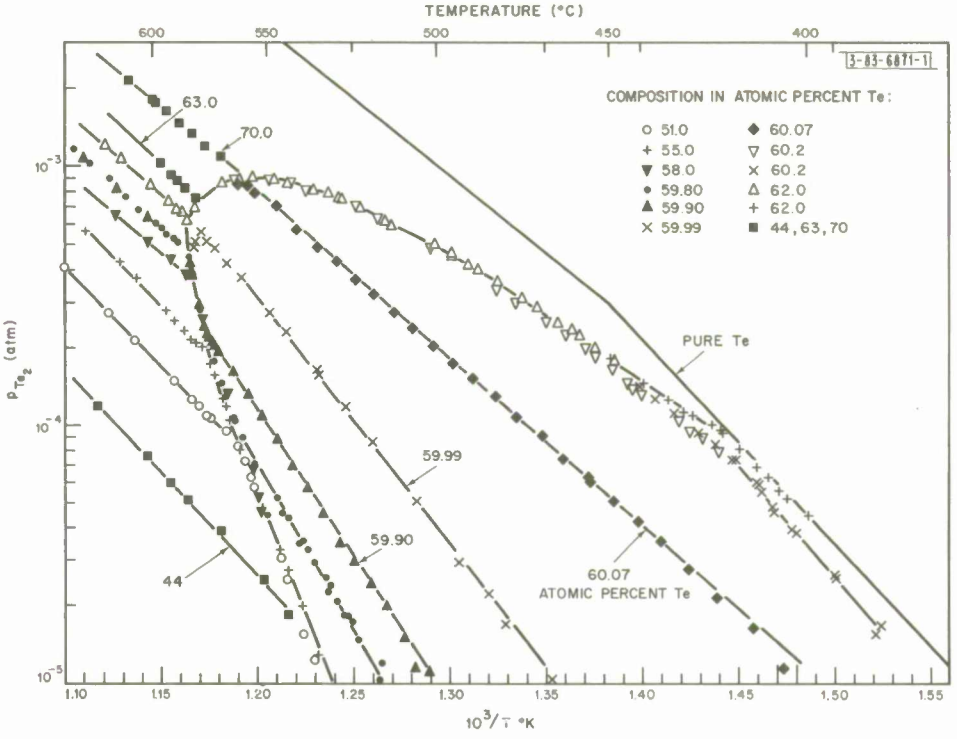

Fig. II-7. Partiol pressure of Te_2 os o function af $10^3/T$, where T is absolute temperoture, for a number of Bi-Te compositions.

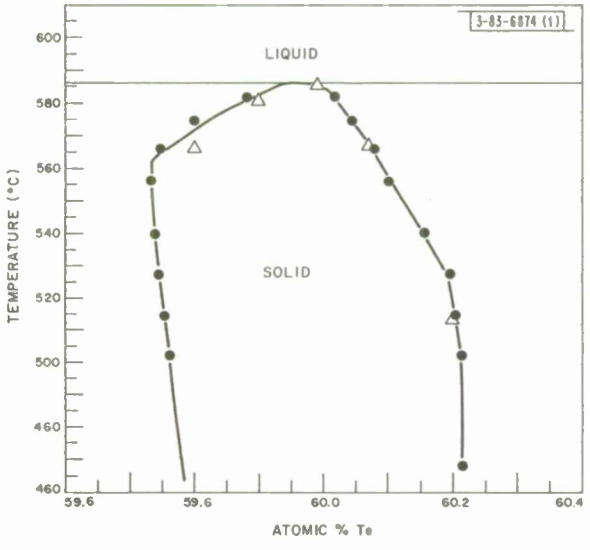

Fig. II-8. Homogeneity ronge for Bi_2Te_3 phase on o plot of temperoture vs otomic percent Te.

in these cases the composition can be unambiguously identified by remembering that p_{Te_2} is larger at a given temperature, the larger the atomic percent Te.

Solidus points for the Bi_2Te_3 phase obtained from the partial pressure data are shown in the T-x projection of Fig. II-8. Points represented by triangles were obtained directly from Fig. II-7, while those represented by circles were found by using isotherms constructed from the data in Fig. II-7. The interpolated maximum melting composition is 59.95 atomic percent Te at 586.0°C. In Table II-3 the solidus points of Fig. II-8 are compared with values calculated by applying the antistructure model to the Hall coefficient data of Satterthwaite and Ure[12] for the crystals that are first to freeze from large volume melts of known composition. Columns 1 and 2 represent Satterthwaite and Ure's results, and columns 1, 3, and 4, ours. The equations used

TABLE II-3
SOLIDUS POINTS FOR Bi_2Te_3(c)

Liquid Composition (atomic percent Te)	Satterthwaite and Ure Apparent Carrier Concentration p* or n* (cm^{-3})	Present Results		Calculated from p* or n* Solid Composition (atomic percent Te)
		T°C	Solid Composition (atomic percent Te)	
50.4	–	565.5	59.980 ± 0.025	–
55.3	–	580.5	59.882 ± 0.012	–
59.0	6×10^{19} p	585.5	(59.942)	59.899
59.95	3.03×10^{19}	586.0	59.95†	59.947
61.1	1×10^{19}	–	–	59.983
62.4	1.3×10^{18}	584.8	59.995	59.998
62.7	intrinsic	584.3	60.001	60.000
63.0	2×10^{18} n	584.0	60.002	60.002
63.9	6×10^{18}	581.7	60.016	60.007
64.4	1×10^{19}	580.3	60.020	60.011
65.3	2×10^{19}	577.8	60.031	60.022
66.0	3.03×10^{19}	576.0	60.037	60.033
60.0	–	566.6	60.074	–

†Estimated maximum melting composition.

to calculate the solidus compositions of column 5 are

$$x_{Te} - 3/5 = 3.38(10^{-23})\,(0.326\,n^*) \qquad n \gg p$$

$$3/5 - x_{Te} = 3.38(10^{-23})\,(0.514\,p^*) \qquad p \gg n$$

where n* and p* are the apparent carrier concentrations at 77°K as determined from the Hall coefficient in the basal plane ($n^*, p^* = 1/e\,R_H$) and where the coefficients 0.326 and 0.514 are proportionality constants, arising from the band structure, which relate the apparent and true carrier concentrations. It is seen that a more extensive comparison is available for the Te-rich, n-type compositions and that for these the agreement between observed and calculated solidus compositions is good. A more detailed characterization of the antistructure defect model requires it to account for the composition and temperature dependence of p_{Te_2} within the Bi_2Te_3 homogeneity range. This is complicated by the fact that Bi_2Te_3 is most likely a degenerate semiconductor at the high temperatures involved. However, it can be said that the simple model valid for a nondegenerate semiconductor, which would require $p_{Te_2}^{1/2} \propto (3/5 - x_{Te})^{-4/5}$ for extrinsic p-type Bi_2Te_3 and $p_{Te_2}^{1/2} \propto (x_{Te} - 3/5)^{4/5}$ for extrinsic n-type Bi_2Te_3, is inadequate.

Data omitted from Fig. II-7 for clarity show that there is a peritectic phase on the Bi-rich side of Bi_2Te_3 which lies somewhere between 55 and 57 atomic percent Te at 540°C and which decomposes at 562 ± 2°C. At 540°C, 58.0 and 59.0 atomic percent Te lie in the three-phase field between this peritectic phase and Bi_2Te_3, while 50 and 55 atomic percent Te lie in the three-phase field between the peritectic phase and a Bi-rich melt. Powder diffraction patterns indicate that the peritectic phase has a structure closely related to, but distinct from, that of Bi_2Te_3.

The optical absorption data for Bi-Te melts have been subjected to a preliminary analysis. It appears that a vapor species detected by optical absorption is BiTe(g) and that its partial pressure over Bi_2Te_3 is about 1/5 p_{Te_2} at 586°C. The partial pressure of Bi is lower than p_{Te_2} by a factor of 4000.

R. F. Brebrick

E. PARTIAL PRESSURES OF Zn AND Te_2 OVER ZnTe

For all compositions within the homogeneity range of ZnTe(c), the partial pressures of Zn, p_{Zn}, and Te_2, p_{Te_2}, over the compound are related by the equation

$$p_{Zn}p_{Te_2}^{1/2} \equiv K = \exp(\Delta G_f^o/RT) \qquad \text{(II-1)}$$

where ΔG_f^o is the Gibbs free energy of formation per mole of ZnTe(c) from Zn(g) and Te_2(g), each at 1 atm. Values of K obtained from the literature scatter over a factor of ten at a given temperature. As a consequence experimental and theoretical investigations of the native point defects in ZnTe are hindered. We have determined the values of p_{Zn} and p_{Te_2} for Zn-saturated and Te-saturated ZnTe(c), respectively, and both pressures for ZnTe that is very nearly congruently subliming. The pressures were found by measuring the optical density of the coexisting vapor between 2100 and 1990 Å, where the optical absorption is due to Te_2(g), and near 2138 Å, where Zn(g) absorbs strongly. In contrast to most of the methods used previously, ours is a static method.

It was found that p_{Zn} over Zn-saturated ZnTe is the same as that over pure Zn(ℓ) up to 910°C within an experimental error of ±2 percent. The value of p_{Te_2} was too small to measure. Over Te-saturated ZnTe, p_{Zn} was too small to measure, while p_{Te_2} is somewhat less than that over pure Te(c,ℓ). At 910°C, p_{Te_2} is 0.37 atm compared to 0.47 atm for pure Te(ℓ). Measurements on a vapor-grown ZnTe crystal gave values for both p_{Zn} and p_{Te_2}, as summarized in Table II-4. The Table shows that with increasing temperature the ratio p_{Zn}/p_{Te_2} reaches the value of 2.0 expected for congruent sublimation, but then drops somewhat below. We believe

TABLE II-4

PARTIAL PRESSURES OF Zn(g) AND Te_2(g) OVER ZnTe(c) FOR COMPOSITIONS WITHIN THE HOMOGENEITY RANGE

$10^3/T°K$	$10^5 \times p_{Zn}$ (atm)	$10^5 \times p_{Te_2}$ (atm)	p_{Zn}/p_{Te_2}	$10^7 \times p_{Zn}p_{Te_2}^{1/2}$ ($atm^{3/2}$)
1.017	4.88	1.065	4.58	1.59
0.9967	8.07	2.17	3.72	3.76
0.9770	11.8	4.60	2.56	8.00
0.9593	17.1	7.30	2.34	14.6
0.9504	21.6	9.14	2.36	20.6
0.9411	29.0	12.3	2.36	32.1
0.9331	33.3	15.2	2.19	41.0
0.9251	38.9	19.2	2.02	53.9
0.9170	47.5	24.2	1.96	73.9
0.9093	55.7	29.9	1.86	96.3
0.9017	68.4	36.5	1.87	130
0.8939	80.1	44.4	1.80	168
0.8870	95.1	53.0	1.79	219
0.8864†	94.6	57.0	1.66	225
0.8795	117	68.0	1.72	305
0.8724	139	77.7	1.79	387
0.8653	170	94.2	1.80	521
0.8594	199	111	1.79	663
0.8565	213	119.6	1.78	736
0.8514	249	135	1.84	915
0.8450	286	154	1.86	1,120
0.8390	325	174	1.87	1,350

†16 haurs at temperature before making measurements.

the discrepancy is due to a combination of experimental error and error in the published vapor pressure for Zn(ℓ). A least squares fit of 22 points gives

$$\log K = -(16{,}350 \pm 68)/T + (9.860 \pm 0.062) \qquad (960° \text{ to } 1190°K) \qquad \text{(II-2)}$$

where the pressures are in atm and the quoted errors are the standard deviations in the slope and intercept. The standard deviation in log K is 0.016. The plot of log K vs $10^3/T$ according to Eq. (II-2) is parallel to but 40 percent below the line of Korneeva, et al.,[14] whose values are the highest thus far obtained. The values obtained by Goldfinger and Jeunehomme[15] are about 55 percent below ours. Those obtained from Lee and Munir[16] or from Reynolds, et al.[17] are about 8 times smaller than ours and have a steeper temperature dependence. Our results and those from the literature are compared in Fig. II-9.

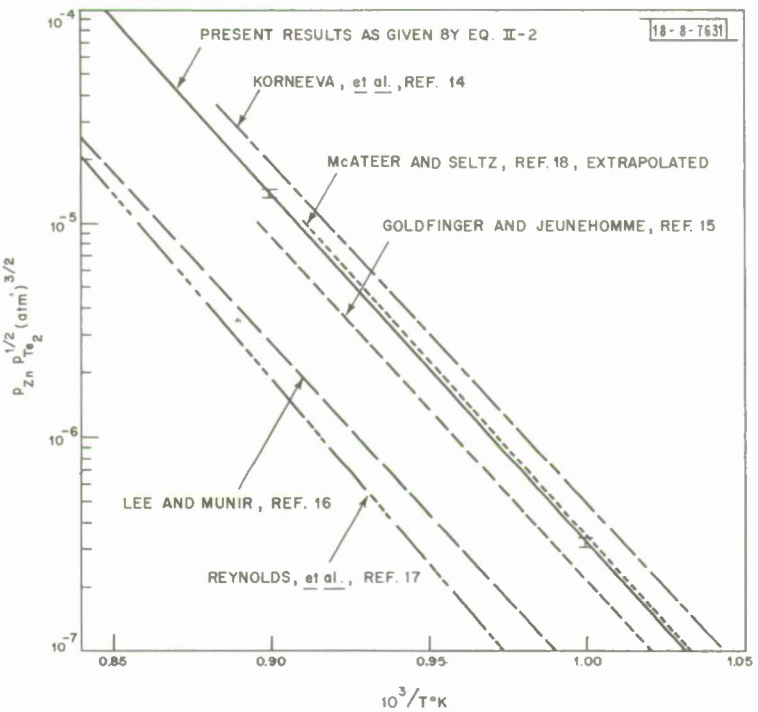

Fig. II-9. Volues of $p_{Zn}p_{Te_2}^{1/2} \equiv K$ for ZnTe plotted on a logarithmic scale ogoinst $10^3/T$. (The totol width of the error bors ot $10^3/T = 1.00$ and 0.90 is twice the stondord deviotion in log K.)

Assuming that the ratio $p_{Zn}/p_{Te_2}^{1/2}$ is the same whether the pressure values for a 50 atomic percent melt or for the pure elements are used (i.e., that the melt belongs to a certain class which contains ideal and regular melts as special cases), the values of p_{Zn} and p_{Te_2} over ZnTe(c) at the maximum melting point, 1563°K, can be calculated. Using Eq. (II-2) we obtain $p_{Zn} = 1.33$ atm, $p_{Te_2} = 0.036$ atm.

The Zn-saturated and Te-saturated ZnTe used in this study were further characterized by determining their lattice parameters, which are listed in Table II-5. The near equality of the

TABLE II-5

LATTICE PARAMETERS FOR ZnTe(c) AT 25°C

Sample	Overoll Campositian (atomic percent Te)	Preparatian	$\sigma(\Delta 2\theta)$ (deg)	$a_a \pm \sigma(a_a)$ (Å)
1	40	a	0.012	6.1026 ± 0.0001
2	40	b	0.014	6.1028 ± 0.0002
3	55	o	0.014	6.1024 ± 0.0001
4	55	c	0.017	6.1023 ± 0.0002
NBS †	Nom. 50	–	0.010	6.1026 ± 0.0001

†Dato of Ref.19 onolyzed by using aur program. Parameter agrees with that af Ref.19.

Column 3 letters denote the following:

o – Synthesized by heoting weighed elements to ~600°C in evocuoted, sealed silica tube; graund ta pass 44 μ stondord sieve; annealed in evocuoted, seoled silica tube for 20 hours at 345°C; quenched in woter.

b – Some as o, except thot onneol at 345°C was replaced by onneal far 2 hours ot 1000°C.

c – Synthesized as in a; onnealed far 120 haurs at 1050°C; quenched in woter; graund to pass 44 μ standard sieve.

parameters indicates the homogeneity range for ZnTe(c) is well under 1 atomic percent wide. The diffraction line positions were obtained with a Philips diffractometer using CuKα_1 radiation (λ = 1.5405 Å) and were corrected using Si and W as external standards. The lattice parameter was found by minimizing the function $R \equiv \left\{ \sum_{i=1}^{n} (2\theta_{i,obs} - 2\theta_{i,calc})^2/(n-1) \right\}^{1/2}$ using a "simplex" computer program written in our Laboratory. The errors quoted for the lattice parameters in Table II-5 are the standard deviations calculated from R and the variance-covariance matrix.

R. F. Brebrick

F. CALCULATION OF SOLIDUS CURVES FOR SEMICONDUCTOR ALLOY SYSTEMS

Whereas liquidus curves in many alloy phase diagrams can be determined quickly and accurately by thermal analysis, the experimental determination of solidus curves is generally more time consuming and subject to error. One method for obtaining solidus curves employs thermal analysis to find the melting temperatures of homogeneous alloys of known composition. Equilibration of such alloys generally requires long annealing times because of the low diffusion rates in the solid state. The other principal method is to determine the composition of the solid frozen from a melt of known composition. To obtain accurate values, it is necessary for crystallization to take place under equilibrium conditions, which are frequently difficult to achieve. Consequently there are many systems for which liquidus curves have been determined but solidus curves are not available. For two such systems, ZnTe-CdTe and ZnTe-ZnSe, we have

used a simple theoretical equation to calculate approximate solidus curves from the published liquidus curves. This equation is based on a simplifying assumption whose validity has been examined by using the equation to calculate solidus curves for a number of similar systems for which both liquidus and solidus curves have been determined experimentally.

For a completely miscible binary system with pure components A and B, the compositions of the liquid and solid phases in equilibrium at temperature T are related by:[20]

$$RT\left(\ell n \frac{X_A^\ell}{X_B^\ell} - \ell n \frac{X_A^s}{X_B^s}\right) = \Delta H_A\left(1 - \frac{T}{T_A}\right) - \Delta H_B\left(1 - \frac{T}{T_B}\right) - D \qquad (II-3)$$

with

$$D = \frac{\partial \Delta G_e^\ell}{\partial X_A^\ell} - \frac{\partial \Delta G_e^s}{\partial X_A^s} \qquad (II-4)$$

where X_i represents the mole fractions of component i in the respective phases, ΔH_i the enthalpy of fusion, and T_i the melting temperature. ΔG_e represents the excess molar free energy of formation of the respective phases.

In terms of the activity coefficients γ, D can be expressed as

$$D = RT\ell n\left(\frac{\gamma_A^\ell}{\gamma_A^s} \cdot \frac{\gamma_B^s}{\gamma_B^\ell}\right) \quad . \qquad (II-5)$$

For ideal solutions, the enthalpies and excess entropies of mixing are zero and $D_{ideal} = 0$. Equation (II-3) then becomes

$$\ell n \frac{X_A^\ell}{X_B^\ell} - \ell n \frac{X_A^s}{X_B^s} = \frac{\Delta H_A}{R}\left(\frac{1}{T} - \frac{1}{T_A}\right) - \frac{\Delta H_B}{R}\left(\frac{1}{T} - \frac{1}{T_B}\right) \quad . \qquad (II-6)$$

For nonideal solutions, the enthalpies and excess entropies of mixing are not zero, and D is generally finite. However, if the deviations from ideality are comparable in the liquid and solid phases, the values of D will be small. This is the case for a number of metallic systems, such as Ag-Au and Cu-Ni, which show no marked minimum in their solidus curves. Values of D for these systems have been calculated from the experimental liquidus and solidus data by means of Eq. (II-3). The small values obtained are consistent with the small values reported by Wagner[21] for the difference between the integral excess free energies of formation, $\Delta G_e^\ell - \Delta G_e^s$, in these systems.

For sufficiently small values of D, reasonably accurate solidus curves can be calculated from experimental liquidus curves and heats of melting by using Eq.(II-6). To determine whether this is likely to be the case for semiconductor alloy systems, the experimental solidus curves for a number of such systems have been compared with the curves calculated by using the equation. For the Ge-Si alloys, the calculated curve is parallel to the experimental curve (obtained by thermal analysis of annealed alloys) but lies above it by about 20°C; this difference might be due in part to experimental errors resulting from incomplete equilibration of the annealed alloys.

For the InSb-GaSb and InAs-GaAs systems, the agreement between the calculated and experimental curves is excellent, although in both cases the calculated values lie somewhat above the experimental ones at compositions approaching the higher melting compound. The discrepancy in this region is even more pronounced in the InSb-InAs system. It is believed that these discrepancies result from the differences in atomic size of the alloying elements, which cause an increase in the strain energy of the solid solutions and therefore lead to larger values of D.

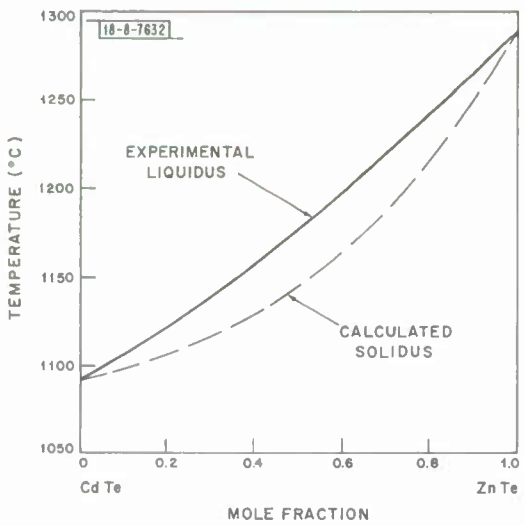

Fig. II-10. Experimental liquidus curve and calculated solidus curve for ZnTe-CdTe system.

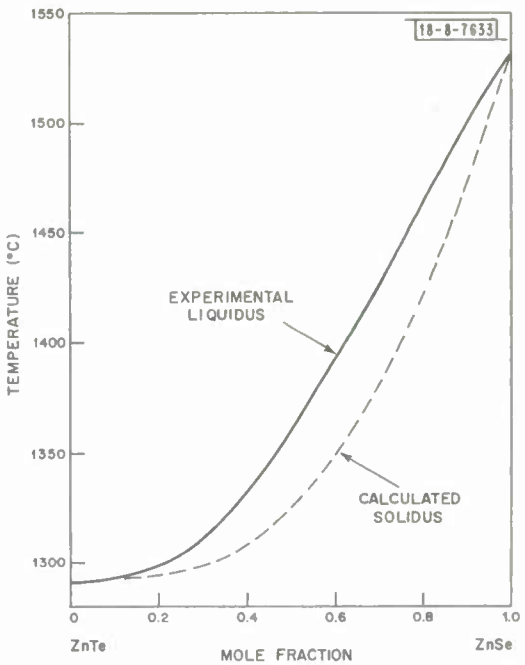

Fig. II-11. Experimental liquidus curve and calculated solidus curve for ZnTe-ZnSe system.

In view of the relatively good agreement between the solidus curves calculated from Eq. (II-6) and experimental data for a number of semiconducting alloy systems, it seems reasonable to use this equation to calculate approximate solidus curves from the liquidus curves for similar systems where reliable solidus data are not yet available. The results of such calculations for the ZnTe-CdTe and ZnTe-ZnSe systems are shown in Figs. II-10 and II-11, respectively. The difference in composition between the liquid and solid solutions in equilibrium at a given temperature is relatively small. This suggests that it may not be very difficult to grow homogeneous alloy single crystals from the melt by controlled directional freezing.

J. M. Steininger

G. EXPERIMENTAL COMPARISON OF HARTREE-FOCK AND SLATER EXCHANGE POTENTIALS IN ALUMINUM

Slater's approximation to the Hartree-Fock exchange operator has been widely used in atomic, molecular and solid state calculations. Using the wave functions from such relativistic Hartree-Fock-Slater (RHFS) calculations, Cromer and Waber[22] have calculated the X-ray scattering factors (i.e., Fourier transform of the electron charge density) for many free atoms and

ions. Similarly, Doyle and Turner[23] have tabulated the scattering factors derived from relativistic Hartree-Fock (RHF) wave functions in which the exchange was calculated exactly. Comparison of the RHFS and RHF calculations shows systematic differences of the order of 1 to 4 percent persisting at large values of the scattering vector $\vec{k}$; that is, in regions of reciprocal space that probe deeply into the atomic core.

Scattering factors of aluminum measured on powders[24] were found to disagree with both theories[25,26] even at large values of $|\vec{k}|$ where solid state effects should not be important. Attempts at resolving the differences by means of a band calculation were unsuccessful.[25] However, results obtained with imperfect single crystals[27] came closer to agreeing with RHF values[23] at large $|\vec{k}|$ (333,511). We have obtained experimental results which successfully distinguish between the two calculations, agreeing with the RHF values for scattering from the closed shell electrons.

Our X-ray measurements were made on cold worked powder pellets using Ni-filtered CuK_α radiation and monitoring the incident beam. To put the results on an absolute scale we used a monochromatic CuK_α incident beam to measure the first three integrated intensities. The incident beam was then counted after attenuation by brass foils. The relative intensities were step-scanned while the absolute intensities were obtained using the open slit technique. Since extinction, porosity and surface roughness are wavelength dependent, all samples were examined by using Mo, Cu and CrK_α radiation; none were used which showed measureable effects. Preferred orientation was studied by forming samples at different pressures. The samples finally used were formed at pressures from 1000 to 5000 psi. Mass spectrographic analysis showed the level of all impurities to be lower than 0.05 molar percent.

The polarization constant of the doubly bent LiF monochromator used in the absolute intensity measurements was determined experimentally by diffraction from a perfect crystal of germanium, as described by Jennings;[28] it was found to be 0.753 ± 0.015. The electronic dead time was measured, and all data were corrected for it. The mass absorption of the sample material was measured on a thin pressed pellet and found to be $50.4 \pm 0.3\,cm^2/g$, in good agreement with a recent value of $50.6\,cm^2/g$ (Ref. 29).

Extremely long counting times were used to obtain a statistical accuracy better than 0.1 percent on all integrated intensities. Great care was taken in determining the background as this can be a major source of error, particularly when peaks lie close together. It was necessary to correct the (331) peak for the presence of a weak absorption edge at nearly the same angle. All peaks were also corrected for thermal diffuse scattering.

The absolute measurement of the first three peaks allowed us to scale the nonmonochromatic relative intensities and obtain the absolute structure factor $|F(k)|$ and hence the atomic form factor $|f(k)|$ in the solid. The correction for thermal vibration was made using a Debye temperature of $386 \pm 2°K$ obtained from the latest X-ray[25] and neutron[30] measurements. The corrections for anomalous dispersion were 0.19 and 0.27 for $\Delta f'$ and $\Delta f''$, respectively.

Our results are presented in Table II-6 along with the form factors from RHF and RHFS calculations. The error intervals given include the uncertainties affecting all the variables entering in the integrated intensity formula. In addition, the results of a measurement on one of our samples by Jennings (Army Research Center, Watertown, Massachusetts) are included. His findings can be seen to agree well with ours on an absolute and relative scale.

TABLE II-6

EXPERIMENTAL AND CALCULATED FORM FACTORS FOR ALUMINUM

hkℓ	$\frac{\lvert\vec{k}\rvert}{4\pi}$	$\lvert F(\vec{k})\rvert^2/\mu$ (this work)	$\lvert F(\vec{k})\rvert^2/\mu$ (Jennings)	f(k) (experimental, this work)	f(k) (RHF)	Δ_{RHF}†	f(k) (RHFS)	Δ_{RHFS}†
111	0.2138	0.5498	0.5482 ± 0.005	8.82 ± 0.06	8.97	−1.7	9.10	−3.2
200	0.2470	0.4864	0.4845 ± 0.004	8.40 ± 0.06	8.51	−1.3	8.63	−2.7
220	0.3493	0.3311	0.3340 ± 0.004	7.29 ± 0.06	7.32	−0.4	7.43	−1.9
311	0.4094	0.2572		6.67 ± 0.06	6.66	+0.1	6.78	−3.0
222	0.4276	0.2374		6.49 ± 0.06	6.47	+0.3	6.59	−1.5
400	0.4937	0.1701		5.78 ± 0.06	5.76	+0.3	5.90	−2.1
331	0.5381	0.1344		5.34 ± 0.06	5.32	+0.4	5.46	−2.2
420	0.5520	0.1244		5.20 ± 0.05	5.18	+0.4	5.33	−2.5
422	0.6047	0.0905		4.67 ± 0.05	4.67	0.0	4.82	−3.2

$\lvert F(k)\rvert^2$ = crystal structure factor, μ = linear absorption coefficient, f(k) = form factor.

†Percentage difference between experimental and calculated values.

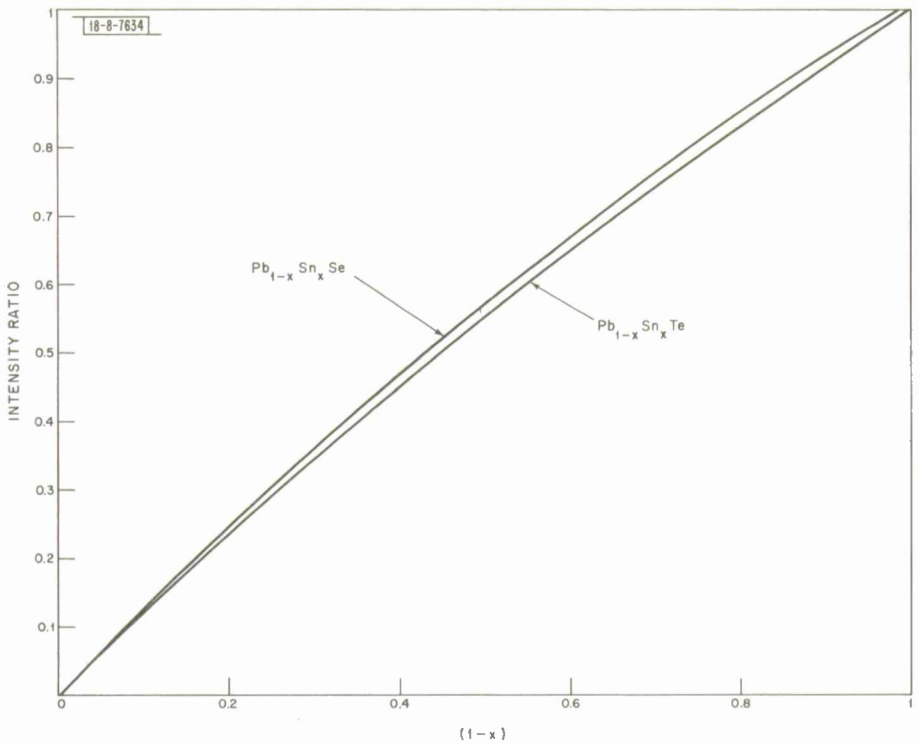

Fig. II-12. Sample-to-standard intensity ratio for X-rays due to Pb excited by electron beam, calculated as a function of $(1-x)$ for $Pb_{1-x}Sn_xTe$ and $Pb_{1-x}Sn_xSe$ alloys. Both alloys are compared with PbTe standard.

TABLE II-7

ANALYSIS OF $(Pb_{1-x}Sn_x)(Te_{1-y}Se_y)$ ALLOYS

Sample		Pb	Sn	Te	Se	Total
1	weight fraction	0.540	0.068	0.384	0.007	0.999
	2 × (atom fraction)	0.820	0.180	0.974	0.026	(2)
2	weight fraction	0.535	0.082	0.360	0.027	1.004
	2 × (atom fraction)	0.789	0.211	0.893	0.107	(2)
3	weight fraction	0.533	0.060	0.326	0.066	0.985
	2 × (atom fraction)	0.837	0.163	0.754	0.246	(2)
4	weight fraction	0.573	0.072	0.291	0.101	1.037
	2 × (atom fraction)	0.820	0.180	0.640	0.360	(2)

The mean values of our measured scattering factors are larger than those of the previous workers[24,25,†] for all peaks, although for most peaks there is some overlap of the error limits. For all but the first two Fourier components, however, our values agree well with the atomic RHF calculation. In other words, for reflections where the dominant contribution is made by the closed shell electrons, agreement with atomic calculations is excellent, as one would expect; the lower values obtained for the first two Bragg peaks are indicative of delocalization of the outer electrons. A solid state calculation could, at least qualitatively, verify this assumption.

The strong departure of the experimental results from the RHFS shows that the Slater exchange potential fails to accurately describe the total core charge density, which is not surprising for two reasons. First, it is known from earlier experiments on rare gases that RHF charge densities agree well for all but He, so that the knowledge that RHFS differs from RHF by more than the experimental error tells us that RHFS charge densities disagree with experiment for those atoms. Secondly, the derivations of one-electron Hamiltonians with a $\rho^{1/3}$ approximation seem to depend on having the charge density varying slowly in space (a questionable proposition, at least for the inner electrons).

P. M. Raccah
V. E. Henrich

H. ELECTRON MICROPROBE ANALYSIS OF $(Pb_{1-x}Sn_x)(Te_{1-y}Se_y)$ ALLOYS

A method has been developed for determining the four major components in $(Pb_{1-x}Sn_x)(Te_{1-y}Se_y)$ alloys by electron microprobe analysis. Intensities of the X-rays excited by the electron beam are measured for the fifth order $L\alpha_1$ line of Pb(λ = 1.175 Å), the third order $L\alpha_1$ line of Sn(λ = 3.600 Å), the third order $L\alpha_1$ line of Te(λ = 3.290 Å), and the fifth order $K\alpha_1$ line of Se(λ = 1.105 Å). Several areas of each sample are examined. The standards used are PbTe for Pb and Te, SnTe for Sn, and PbSe for Se.

The available quantity of quaternary alloys is insufficient to permit experimental calibration of the microprobe analysis. Therefore a calculated calibration is made by using the backscattered electron correction of Duncomb and Shields,[32] the ionization correction of Nelms,[33] and the adsorption correction of Philibert.[34] For a given value of $(1 - x)$, the intensity of Pb radiation is found to be almost independent of the Te/Se ratio, since this intensity is almost the same for $Pb_{1-x}Sn_xTe$ as for $Pb_{1-x}Sn_xSe$ (see Fig. II-12). In analyzing a quaternary sample, an approximate value of $(1 - x)$ is first obtained from the sample-to-standard intensity ratio for Pb radiation by using the calibration curve for $Pb_{1-x}Sn_xTe$ in Fig. II-12. Approximate values for $(1 - y)$ and y are then obtained from the intensity ratios for Se and Te, respectively, by using calibration curves calculated for the estimated value of $(1 - x)$. Using these approximate values, a new correction factor is calculated for each of the four elements, and this factor is used to obtain the weight fraction of the element from its intensity ratio. The atom fractions of all four elements are then calculated and used to obtain new correction factors. This procedure is continued until convergence occurs. Three steps are usually sufficient. The results obtained in this manner for four representative quaternary alloys are given in Table II-7. [The values of $(1 - x)$, x, $(1 - y)$, and y are designated in the table by "2 × (atom fraction)." These values have been adjusted to satisfy the condition that the sum of the atom fractions of both Pb and Sn, and Te and Se, must equal 0.5.]

M. C. Finn

† Absolute measurements of the first three scattering factors of Al on powder in transmission have recently been reported.[31] As in our case, agreement is claimed with both powder and single crystal data.

REFERENCES

1. A. C. Prior, J. Sci. Instr. 38, 198 (1961).
2. A. Rabenau (private communication).
3. R. V. Pisarev, I. G. Sinii, and G. A. Smolenskii, Sov. Phys.—Solid State 9, 80 (1967).
4. S. R. Chinn and H. J. Zeiger, Phys. Rev. Letters 21, 1589 (1968).
5. G. A. Smolenskii, V. M. Yudin, P. P. Syrnikov, and A. B. Sherman, Sov. Phys. —Solid State 8, 271 (1967).
6. J. M. Longo and J. A. Kafalas, Mat. Res. Bull. 3, 687 (1968).
7. J. M. Longo and J. A. Kafalas, J. Appl. Phys. (to be published, March 1969).
8. R. D. Shannon and C. T. Prewitt, Acta Cryst. (to be published).
9. Z. Boncheva-Mladenova, A. S. Pashinkin, and A. V. Novoselova, Inorg. Mater. 2, 1324 (1966).
10. S. I. Gorbov and A. V. Krestovnikov, Inorg. Mater. 2, 1465 (1966).
11. G. R. Miller and L. Che-Yu, J. Phys. Chem. Solids 26, 173 (1965).
12. C. B. Satterthwaite and R. W. Ure, Jr., Phys. Rev. 108, 1164 (1957).
13. R. F. Brebrick, J. Phys. Chem. 72, 1032 (1968).
14. I. V. Korneeva, A. V. Belyaev, and A. V. Novoselova, Russ. J. Inorg. Chem. 5, 1 (1960).
15. P. Goldfinger and M. Jeunehomme, Trans. Far. Soc. 59, 2851 (1963).
16. W. T. Lee and Z. A. Munir, J. Electrochem. Soc. 114, 1236 (1967).
17. R. A. Reynolds, D. G. Stroud, and D. G. Stevenson, J. Electrochem. Soc. 114, 1281 (1967).
18. J. H. McAteer and H. Seltz, J. Amer. Chem. Soc. 58, 2081 (1936).
19. H. E. Swanson, M. C. Morris, E. H. Evans, and L. Ulmer, Standard X-ray Diffraction Powder Patterns, U. S. National Bureau of Standards Mono. 25, Sec. 3 (July 1964), p. 38.
20. A. Prince, Alloy Phase Equilibria (Elsevier, Amsterdam, 1966), p. 48.
21. C. Wagner, Acta Met. 2, 242 (1954).
22. D. T. Cromer and J. T. Waber, Acta Cryst. 18, 104 (1965).
23. P. A. Doyle and P. S. Turner, Acta Cryst. A24, 390 (1968).
24. B. W. Batterman, D. R. Chipman, and J. J. DeMarco, Phys. Rev. 122, 68 (1961).
25. F. J. Arlinghaus, Phys. Rev. 153, 743 (1967).
26. L. M. Sachs, Acta Cryst. 22, 931 (1967).
27. J. J. DeMarco, Phil. Mag. 15, 483 (1967).
28. L. D. Jennings, Acta Cryst. A24, 472 (1968).
29. G. D. Hughes, J. B. Woodhouse, and I. A. Bucklow, Brit. J. Appl. Phys. (J. Phys. D) 1, 695 (1968).
30. D. L. McDonald, Acta Cryst. 23, 185 (1966).
31. M. Jarvinen, M. Merisalo, and O. Inkinen, Phys. Rev. (to be puhlished).
32. P. Duncumb and P. K. Shields, Proceedings of the Electron Microprobe Symposium (John Wiley and Sons, Inc., New York, 1966), p. 284.
33. A. T. Nelms, Natl. Bur. Standards Circular 577 (1956) and Supplement (1958).
34. J. Philibert, Proceedings of the Third International Symposium on X-ray Optics and X-ray Microanalysis (Academic Press, Inc., New York, 1964), p. 379.

III. PHYSICS OF SOLIDS

A. ELECTRONIC BAND STRUCTURE AND ELECTRONIC PROPERTIES

1. Magneto-Optical Investigation of Bi-Sb Alloys†

The continuing study by magnetoreflection of the band structure in Bi-Sb alloys has now been complemented by measurements in 2- and 5-percent antimony alloys;‡ with these additional alloys we now place the zero energy gap at a composition of ~5-percent antimony.

Our measurements indicate the motion of some of the energy bands in the alloys and permit us to identify the L-point energy bands involved in optical transitions in pure bismuth with those involved in observed transitions in pure antimony. These results suggest a scheme for the variation of the energy bands at the L- and T-points in the Brillouin zone for the bismuth-antimony-arsenic system in which spin-orbit interaction appears to be the primary variable and which is consistent with the previous magnetoreflection results in pure bismuth, antimony and arsenic.

Details of this research will be published.

E. J. Tichovolsky
J. G. Mavroides
D. F. Kolesar

2. Reflectance of EuO

As part of our program for studying the properties of the ferromagnetic semiconductor EuO, we have measured the reflectance from 1 to 11 eV at 300° and 77°K. The 300°K data, shown in Fig. III-1 is very similar to that of Grant and Suits.[1] At 77°K the 1.62 eV peak shifts to 1.52 eV and narrows; the 4.75 eV peak also narrows slightly. The prominent 1.62 eV peak would appear to be due to a single oscillator-like absorption but index of refraction data[2] do not fit such a model. We are presently performing a Kramers-Kronig analysis of the reflectance data to obtain the dielectric constant. Upon obtaining these parameters, we will be able to compare our data with energy band calculations[3] in order to further elucidate the band structure of EuO and related materials.

W. J. Scouler
J. Feinleib
J. O. Dimmock

3. Polaron Zeeman Effect in AgBr

The 168 cm^{-1} ultraviolet induced absorption line in AgBr, which has been previously assigned to a 1s-2p transition of a bound polaron,[4] has been examined at liquid helium temperatures in magnetic fields ($\vec{H} \leqslant 32$ kG) applied perpendicular to the infrared light beam. Just as in the classical Zeeman effect, when the light is polarized perpendicular to $\vec{H}$, the line is split by the magnetic field; when the light is polarized parallel to $\vec{H}$, the line is unchanged to the first order. Figure III-2 shows the splitting of the line, relative to the zero field value. The solid lines in Fig. III-2 represent an empirical fit to the data of the form

† This experiment was carried out using the high field facilities of the Francis Bitter National Magnet Laboratory, M.I.T.
‡ We are grateful to Dr. W. M. Yim of RCA for supplying us with these alloys.

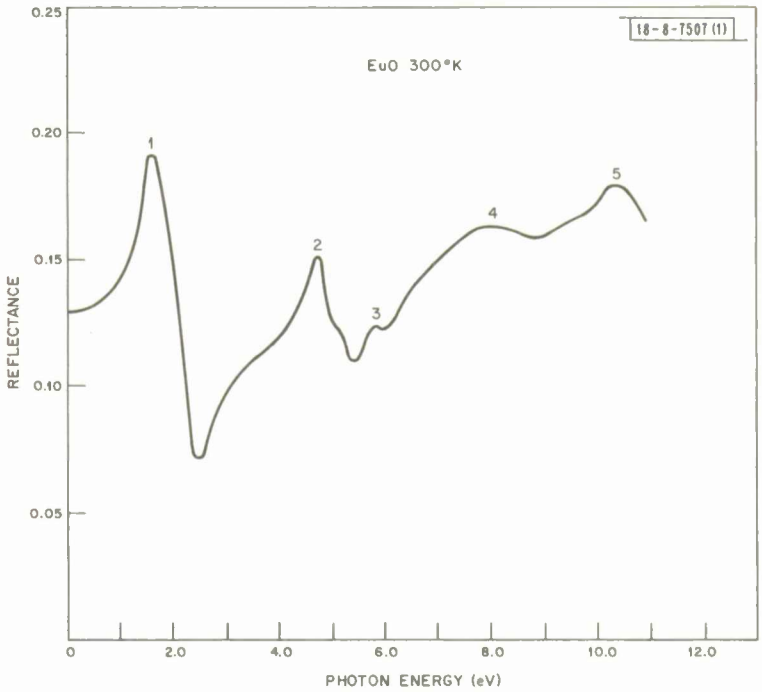

Fig. III-1. Reflectance of EuO at 300°K.

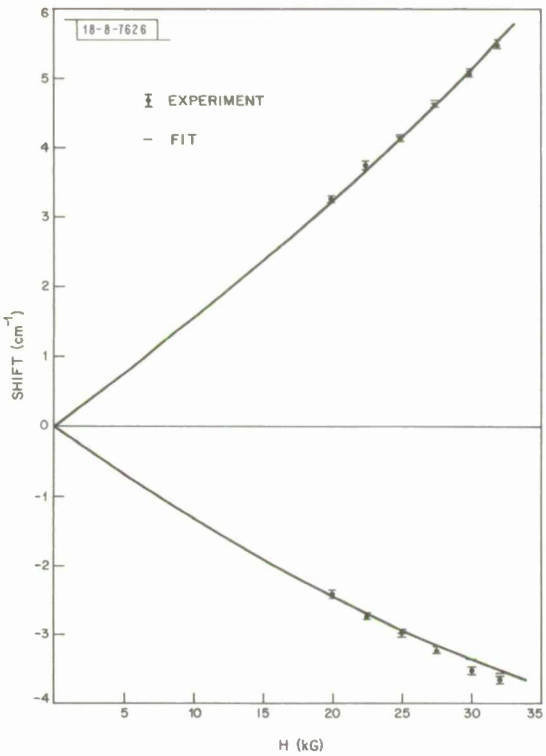

Fig. III-2. Splitting with magnetic field of the 168 cm^{-1} induced absorption line in AgBr.

$$\Delta E = \pm aH + bH^2 \qquad \text{(III-1)}$$

for the shifts observed when the light is polarized perpendicular to $\vec{H}$. A calculation of the effective mass of the polaron, assuming the constant a is given by $e\hbar/2m^*c$, yields $m^*/m = 0.32 \pm 0.01$. The value of b obtained above, 0.0008 cm^{-1}/kG^2, is about the same as that obtained from a simple calculation of the quadratic Zeeman effect for a 2p, $m_\ell = \pm 1$ bound polaron state.

R. C. Brandt
P. P. Crooker
G. B. Wright

4. Tunneling Studies on PbTe and GaAs

We have initiated a study of electron tunneling through insulating films into PbTe with emphasis on the effects of the optic phonons. Metal-insulator-semiconductor devices are being prepared using single crystal samples with thin evaporated oxide films and metal electrodes. Preliminary results have been obtained using SiO_2 and Al_2O_3 films on PbTe and platinum Schottky barriers on p-GaAs. Equipment has been assembled to display the current-voltage (I-V) characteristics, the conductance (dI/dV) and the second derivative of the I-V characteristic (d^2I/dV^2). The GaAs devices show sharp structure in the d^2I/dV^2 data at the LO phonon energy (36.8 meV at 1.5°K). Preliminary data on p-type PbTe show similar structure near the LO phonon energy.

K. W. Nill
J. N. Walpole†

5. Finite Temperature Single-Particle Approximation for Bosons

The standard thermal Hartree-Fock approximation (STHFA) has recently been generalized into a form, the thermal single-determinant approximation (TSDA),[5-7] which deals more satisfactorily with entropy in the zero-temperature limit (that is, with ground state degeneracy) than does the STHFA. In the TSDA the density operator ρ is assumed to be diagonal in the occupation number representation. One seeks a ρ for which $F(\rho)$, the free energy functional for the grand canonical ensemble, is minimum. A necessary condition, which has been discussed in some detail,[5-7] is that $F(\rho)$ be stationary with respect to small variations of ρ.

Here we note that the same approach can be used for a boson system. The density operator is assumed, as in the fermion case, to have the form

$$\rho = \exp[-\beta(\tilde{H} - \mu N)]/\mathrm{Tr}\, \exp[-\beta(\tilde{H} - \mu N)] \qquad \text{(III-2)}$$

The stationarity condition requires that $\tilde{H}$ be the part $E(.\,, N_i, .\,)$ of the Hamiltonian

$$H = \sum f_{ij} c_i^+ c_j + \frac{1}{2} \sum v_{ij,k\ell} c_i^+ c_j^+ c_\ell c_k \qquad \text{(III-3)}$$

diagonal in the occupation number representation. In the boson case

$$E(.\,, N_i, .\,) \equiv \sum f_{ii} N_i + \frac{1}{2} \sum \hat{v}_{ij,ij} [N_i N_j - \frac{1}{2} \delta_{ij} (N_i^2 + N_i)] \qquad \text{(III-4)}$$

where the N_i are the occupation numbers and $\hat{v}_{ij,k\ell} = v_{ij,k\ell} + v_{ij,\ell k}$.

† Department of Electrical Engineering, Massachusetts Institute of Technology, Cambridge, Massachusetts.

The orbitals ψ_i defining the occupation number representation are required to satisfy

$$(\overline{N}_i - \overline{N}_j)\, t_{ij} + \sum_k \hat{v}_{ik,jk} \overline{(N_i - N_j)\, N_k} + \frac{1}{2} [\hat{v}_{ii,ij} \overline{N_i(N_i - 1)} - \hat{v}^*_{jj,ji} \overline{N_j(N_j - 1)}] = 0 \qquad \text{(III-5)}$$

where $\overline{A} \equiv \mathrm{Tr}\rho A$. For fermions, $\hat{v}_{ij,k\ell} \equiv v_{ij,k\ell} - v_{ij,\ell k}$, so that in Eq. (III-4) the diagonal interaction terms and in Eq. (III-5) the terms in square brackets do not appear; Eqs. (III-4) and (III-5) thus reduce to those given previously[5-7] for fermions.

W. H. Kleiner

B. MAGNETISM

1. Nuclear Linewidth Measurements of Mn^{55} in Antiferromagnetic $CsMnF_3$ and $RbMnF_3$

In magnetic media the nuclear spins are coupled by the long-range Suhl-Nakamura[8,9] (S-N) indirect interaction. This interaction is important at low temperatures in compounds containing a high concentration of nuclear spins and possessing small magnetic anisotropy fields, i.e., low electron spin resonance frequencies. Physically, the S-N effect arises from the distortion via hyperfine interaction of the electron spin arrangement when a nuclear spin is tipped through a small angle with respect to the electron magnetization. This distortion is of small amplitude, but because of its long range it reacts on the motion of many other nuclear spins. In suitable compounds, depending on magnetic field intensity and on temperature, this results in a significant correction to the usual nuclear resonance frequency. This correction is the so-called "frequency pulling."

A second general result of the S-N interaction is that the modified nuclear spin wave spectrum provides a significant relaxation mechanism for the spins with a consequent contribution to the nuclear resonance linewidth. Given the form of the nuclear spin wave spectrum, the contribution to the linewidth can be calculated in the frequency-magnetic field regime where the frequency pulling is small compared to the predicted S-N linewidth. In the region where the pulling becomes sufficiently strong so that the above criterion is weakly violated, nondegeneracies in the spin wave spectrum become important in determining the linewidth.[10] In the region of strong pulling, inhomogeneities in the electronic spin wave system become the predominant linewidth-contributing mechanism.[11]

To date, there has been no report in the literature of sufficiently detailed nuclear linewidth measurements to allow an interpretation of the linewidth behavior in terms of existing theories. We have therefore measured the nuclear resonance linewidth of Mn^{55} in the low anisotropy antiferromagnetic compounds $CsMnF_3$ and $RbMnF_3$ by direct observation of the nuclear resonance from 2.5 kOe to 23.5 kOe, at 1.8°K and at 4.2°K. Three samples of each compound, obtained from different sources, have been studied. The "goodness" of the samples was verified by a comparison of the theoretical and experimental dependences of the nuclear frequency, over a 200-MHz range, on magnetic field and on temperature.

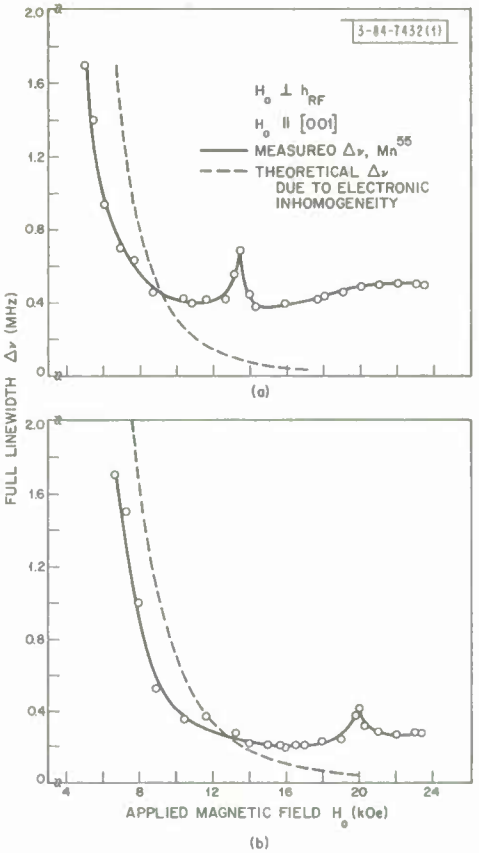

Fig. III-3. Comporison of meosured field dependence of Mn^{55} nucleor linewidth $\Delta\nu$ in $RbMnF_3$ with the contribution to $\Delta\nu$ due to electronic inhomogeneities which ore ossumed responsible for the meosured ontiferromognetic linewidth of 150 Oe ot x-bond for (o) T = 4.2°K, (b) T = 1.79°K.

For case of interpretation, the magnetic behavior of the linewidth, shown in Fig. III-3, is divided into three regions. In the high-field region (20 to 23.5 kOe), where the frequency pulling is weak, the linewidth is interpreted solely in terms of the S-N effect. There is fair agreement between experiment and theory. As the intermediate-field region is approached, the non-degeneracy of the spin wave modes causes a gradual narrowing of the linewidth (except for an anomalous peak). This narrowing effect and the increase, with decreasing magnetic field, of electronic inhomogeneity broadening account for the linewidth behavior in this region of intermediate field. Below about 9 kOe the electronic inhomogeneities, acting through the frequency pulling mechanism, become the predominant line-broadening mechanism. Similar behavior was observed in all samples of both materials. An unexplained anomalous peak in the linewidth curves for $RbMnF_3$, but not $CsMnF_3$, occurs at 678.5 MHz at both temperatures.

Details of this work have been submitted for publication.

R. Weber
M. H. Seavey†

2. Spin-Space Group Analysis of $^4A_2 - {}^2E$ Excitons in Cr_2O_3

The concept of the spin-space group was introduced by Brinkman and Elliott[12] to describe the symmetry of the Heisenberg spin Hamiltonian, a symmetry which is generally higher than

† Air Force Cambridge Research Laboratory, Bedford, Massachusetts.

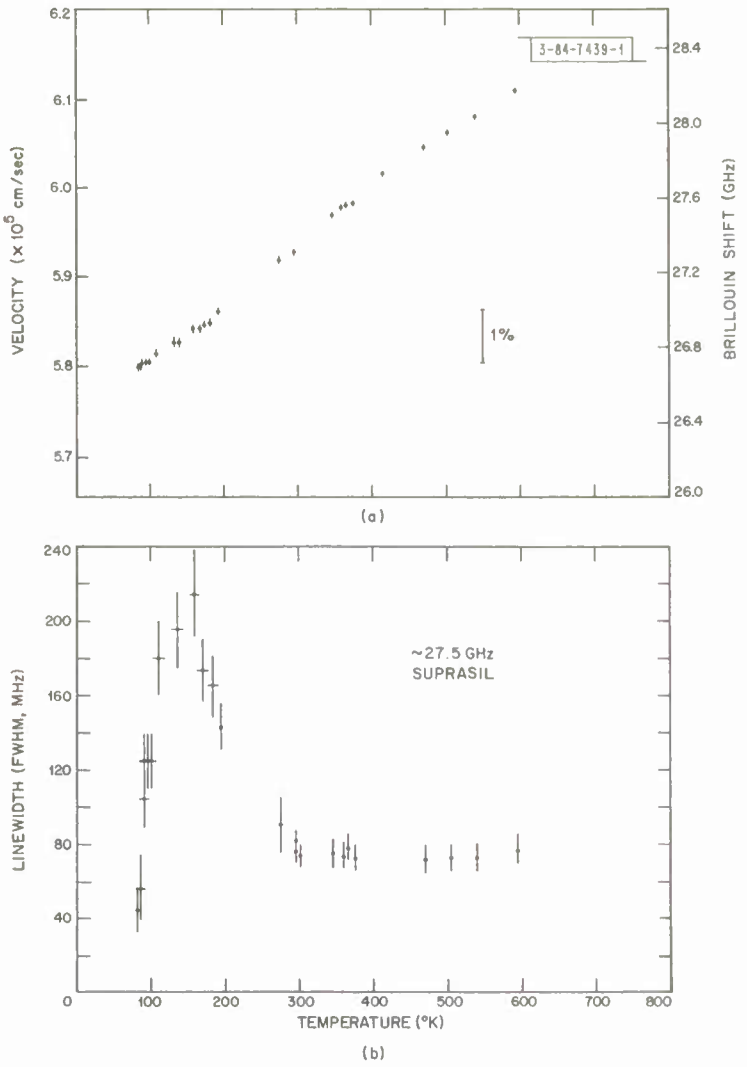

Fig. III-4. (a) Variation with temperature of the velocity and Brillouin shift of longitudinal acoustic phonons in fused quartz. (b) Variation with temperature of the damping of longitudinal hypersonic waves in fused quartz.

that allowed by the magnetic space group. This extra symmetry takes the form of certain independent spin rotations and arises because no orbital operators appear in the spin Hamiltonian, which is, in turn, a reflection of the fact that the spin Hamiltonian can be regarded as a projection of the actual Hamiltonian onto a subspace of states where spin and orbital effects can be separated. This idea extends to cases where the optical excitons of a magnetic insulator are describable by a set of states where spin and orbital effects can be separated, or nearly separated, and has been applied to the $^4A_2 \rightarrow {}^2E$ excitons in Cr_2O_3 to investigate the role of spin-orbit coupling in producing the small but nonzero values that are measured for transfer-of-excitation matrix elements between opposite spin sublattices.[13] This is of interest because there has been difficulty in finding a mechanism of sufficient size, not only in Cr_2O_3 but in other chromium compounds, such as $LaCrO_3$.

Using the group that results from assuming that the excitons can be described by single-ion states which neglect the effects of spin-orbit coupling, it is found that the matrix elements must be zero. Since the matrix elements are not required to be zero by the group that is appropriate if the excitons are described by states including spin-orbit effects, it can be concluded that a suitable mechanism must contain spin-orbit coupling in an essential way. It is probable that this conclusion will not be restricted only to Cr_2O_3. Further applications of the spin-space group idea to optical excitons are planned.

J. W. Allen

C. LASER SCATTERING AND NONLINEAR EFFECTS

1. Brillouin Scattering Study of Acoustic Attenuation in Fused Quartz

The velocity and attenuation of 27- to 28-GHz longitudinal hypersonic waves in fused quartz have been measured for temperatures between 80° and 600°K. The data were obtained using high resolution signal averaging techniques of thermal Brillouin spectroscopy. As shown in Fig. III-4(a) the velocity, or Brillouin shift, increases with temperature at a rate of ~0.011%/°K throughout the range. The attenuation, or linewidth, however, goes through a pronounced peak at a temperature of ~130°K [(Fig. III-4(b))]. Both of these characteristics are in marked contrast to those found previously in crystalline quartz.[14] This sort of behavior usually indicates a structural relaxation mechanism for the hypersonic damping as has been suggested from ultrasonic measurements in fused quartz.[15] However, we have demonstrated in a more complete article[16] that an anharmonic model involving three-phonon interaction can explain the absorption data with fewer adjustable and more justifiable parameters.

A. S. Pine

2. Raman Scattering by Magnetic Excitations in $RbNiF_3$

We have continued our investigation of the magnetic properties of the transparent hexagonal ferrimagnet $RbNiF_3$. Using exchange constants obtained from optical absorption[17] and Raman scattering[18] experiments, we have used several theoretical models to predict the magnetic behavior of $RbNiF_3$, and compared the result with experiment. In particular, the result of a classical Bethe-Peierls-Weiss calculation, using the two dominant ferro- and antiferromagnetic exchange interactions as well as the weaker second nearest neighbor antiferromagnetic

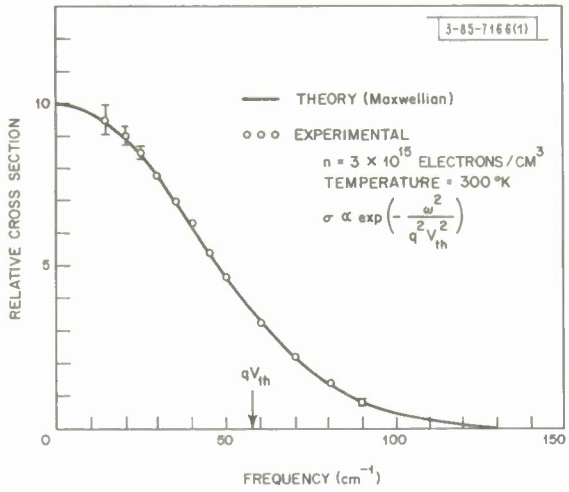

Fig. III-5. Comparison between theory ond experiment of single particle scottering cross section lineshope for electrons in GoAs, $n = 3 \times 10^{15}$ cm^{-3} ot room temperoture; the theory ossumes o thermolized Maxwellian distribution.

Fig. III-6. Comparison between theory ond experiment of single particle scottering cross section lineshope for both light ond heovy holes in GaAs.

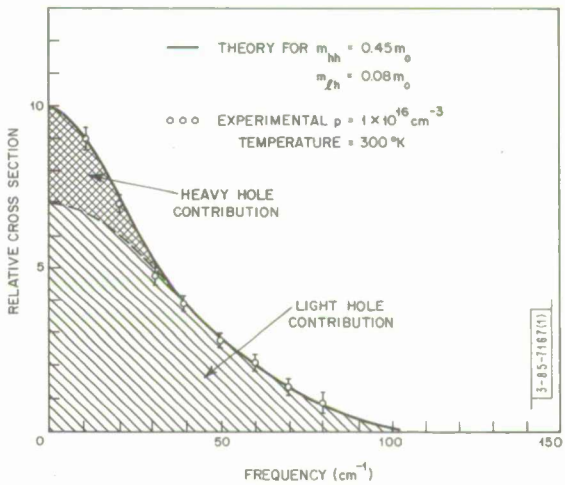

interaction, gives a Curie temperature of 135°K compared to the measured value of 139°K. Also, the temperature at which the A sublattice (with one-half as many sites as the B sublattice) reverses sign in an applied magnetic field in the paramagnetic region, is given within 7 percent. The absolute sublatticc magnetizations as functions of temperature in the paramagnetic region in a magnetic field are also in excellent quantitative agreement with NMR results.[19] Work is now being done on a quantum mechanical B-P-W calculation to help confirm the validity of the classical results.

In order to clarify our understanding of the details of the Raman scattering experiments in $RbNiF_3$, we are examining the selection rules for two-magnon optical scattering and the effects of magnon-magnon interactions in shifting the energy spectrum and altering scattering linewidths.

S. Chinn
H. J. Zeiger

3. Determination by Light Scattering of Carrier Velocity Distributions in Semiconductors

Recently,[20,21] light scattering from single particle electron and hole excitations has been observed in semiconductors using a YAG:Nd^{3+} laser. The scattering arises primarily from electron density fluctuations[21] for GaAs in the limit $\omega_p < qv_t$, where ω_p is the plasma frequency, q is the momentum change imparted to the electron, and v_t is the thermal velocity. In this case, it can be shown that in the limit of infinite relaxation time the cross section is proportional to the electron velocity distribution function, $f(\omega/qv_t)$ for a Maxwellian distribution. Figure III-5 shows a good fit between the calculated and measured cross sections for a Maxwellian electron gas in thermal equilibrium at room temperature.

Scattering from both the light and heavy holes in p-type GaAs at room temperature was also observed as is shown in Fig. III-6, and could be fitted with two superimposed Maxwellian velocity distributions that were calculated using the values of light and heavy hole masses as determined from magneto-optical studies.

Present experiments are under way to investigate nonequilibrium velocity distributions in the presence of an externally applied electric field. A more detailed account of this work is presented in a forthcoming publication.[21]

A. Mooradian

4. Effect of the Molecular Interaction Between Anisotropic Molecules on the Optical Kerr Effect. Field-Induced Phase Transition (Abstract of paper accepted for publication in The Physical Review)

"The effect of molecular interaction between anisotropic molecules in liquids on the nonlinear refractive index is studied. The model, without the driving term describing the strong optical field molecular reorientation, is the same as the Maier and Saupe model of the isotropic to nematic phase transition in liquid crystals. The local field corrections are analyzed with the Onsager theory, the average polarizability being given by the Lorentz-Lorenz formula. It is found that the temperature dependence of the nonlinearity is modified and becomes $(T-T_i)^{-1}$ and that the electric field required to achieve a certain nonlinear index change can be very much smaller than required when only molecular reorientation is considered. Under certain restrictive conditions the liquid can be driven into a new ordered phase, similar to a liquid crystal mesophase."

J. Hanus

REFERENCES

1. P.M. Grant and J.C. Suits (to be published).
2. P. Wachter, Phys. Kondens. Materie 8, 80 (1968).
3. S.J. Cho, private communication.
4. R.C. Brandt and F.C. Brown, Localized Excitations in Solids, edited by R.W. Wallis (Pergamon Press, New York, 1968), p. 322.
5. Solid State Research Report, Lincoln Laboratory, M.I.T. (1968:2), p. 53, DDC 672961.
6. T.A. Kaplan, Bull. Am. Phys. Soc. 13, 386 (1968).
7. T.A. Kaplan and P.N. Argyres (to be published).
8. H. Suhl, Phys. Rev. 109, 606 (1968).
9. T. Nakamura, Progr. Theoret. Phys. (Kyoto) 20, 542 (1958).
10. P.M. Richards, Phys. Rev. 173, 581 (1968).
11. A. Nakamura, V. Minkiewicz and A.M. Portis, J. Appl. Phys. 35, 842 (1964).
12. W.F. Brinkman and R.J. Elliott, Proc. Royal Soc. A294, 343 (1966).
13. J.W. Allen, R.M. Macfarlane and R.L. White, Phys. Rev. (to be published).
14. A.S. Pine, Light Scattering in Solids, edited by G.B. Wright (Springer-Verlag, New York, 1969).
15. O.L. Anderson and H.E. Bommel, J. Amer. Ceramic Cos. 38, 125 (1955).
16. A.S. Pine (to be published).
17. G. Zanmarchi and P.F. Bongers, Solid State Commun. 6, 27 (1968).
18. S.R. Chinn and H.J. Zeiger, Phys. Rev. Letters 21, 1589 (1968).
19. G.A. Smolensky, M.P. Petrov, V.V. Moskalev, V.S. L'vov, V.S. Kasperovich and E.V. Zhirnova, Fiz. Tverd. Tela 10, 1305 (1968).
20. A. Mooradian, Phys. Rev. Letters 20, 1102 (1968).
21. A. Mooradian, Light Scattering in Solids, edited by G.B. Wright (Springer-Verlag, New York, 1969).

DOCUMENT CONTROL DATA – R&D

(Security classification of title, body of abstract and indexing annotation must be entered when the overall report is classified)

1. ORIGINATING ACTIVITY *(Corporate author)* Lincoln Laboratory, M.I.T.	2a. REPORT SECURITY CLASSIFICATION Unclassified 2b. GROUP None

3. REPORT TITLE

Solid State Research

4. DESCRIPTIVE NOTES *(Type of report and inclusive dates)*

Quarterly Technical Summary – 1 November 1968 through 31 January 1969

5. AUTHOR(S) *(Last name, first name, initial)*

McWhorter, Alan L.

6. REPORT DATE	7a. TOTAL NO. OF PAGES	7b. NO. OF REFS
15 February 1969	68	95

8a. CONTRACT OR GRANT NO. AF 19(628)-5167 b. PROJECT NO. 649L c. d.	9a. ORIGINATOR'S REPORT NUMBER(S) Solid State Research (1969:1) 9b. OTHER REPORT NO(S) *(Any other numbers that may be assigned this report)* ESD-TR-69-12

10. AVAILABILITY/LIMITATION NOTICES

This document has been approved for public release and sale; its distribution is unlimited.

11. SUPPLEMENTARY NOTES None	12. SPONSORING MILITARY ACTIVITY Air Force Systems Command, USAF

13. ABSTRACT

This report covers in detail the solid state research work at Lincoln Laboratory for the period 1 November 1968 through 31 January 1969. The topics covered are Solid State Device Research, Materials Research, and Physics of Solids.

14. KEY WORDS

solid state devices
materials research
electronic band structure
magnetism
crystal growth
rare-earth compounds
magneto-optical research
laser scattering
Raman scattering
Brillouin scattering
ion implantation